3-D optogenetic control of arteriole diameter *in vivo*

Philip J. O'Herron[1,8,#], David A. Hartmann[2,8], Kun Xie[1], Prakash Kara[3,4,8], and Andy Y. Shih[5,6,7,8]

[1] Department of Physiology, Augusta University, Augusta, Georgia, USA.

[2] Department of Neurology & Neurological Sciences, Stanford University, Stanford, California, USA.

[3] Department of Neuroscience, University of Minnesota, Minneapolis, Minnesota, USA.

[4] Center for Magnetic Resonance Research, University of Minnesota, Minneapolis, Minnesota, USA.

[5] Center for Developmental Biology and Regenerative Medicine, Seattle Children's Research Institute, Seattle, Washington, USA.

[6] Department of Pediatrics, University of Washington, Seattle, Washington, USA.

[7] Department of Bioengineering, University of Washington, Seattle, Washington, USA.

[8] Department of Neuroscience, Medical University of South Carolina, Charleston, South Carolina, USA.

[#] Corresponding author: poherron@augusta.edu

Correspondence: Philip O'Herron Ph.D.
Department of Physiology
Augusta University
1462 Laney Walker Blvd
CA-2094
Augusta GA 30912

Office: (706) 721-9103
Fax: (706) 721-7299
Email: poherron@augusta.edu

Abstract

Modulation of brain arteriole diameter is critical for maintaining cerebral blood pressure and controlling regional hyperemia during neural activity. However, studies of hemodynamic function in health and disease have lacked a method to control arteriole diameter independently with high spatiotemporal resolution. Here, we describe an all-optical approach to manipulate and monitor brain arteriole contractility in 3-dimensions using combined *in vivo* two-photon optogenetics and imaging. The expression of the red-shifted excitatory opsin, ReaChR, in vascular smooth muscle cells enabled rapid and repeated vasoconstriction controlled by brief light pulses. Two-photon activation of ReaChR using a spatial light modulator produced highly localized constrictions when targeted to individual arterioles within the neocortex. We demonstrate the utility of this method for examining arteriole contractile dynamics and creating transient focal blood flow reductions. Additionally, we show that optogenetic constriction can be used to reshape vasodilatory responses to sensory stimulation, providing a valuable tool to dissociate blood flow changes from neural activity.

Introduction

The brain is a metabolically demanding organ, consuming 20% of the body's energy supply despite being only 2% of its weight (Clark and Sokoloff, 1999; Raichle and Gusnard, 2002). To ensure an adequate supply of oxygen and nutrients, brain arterioles dilate transiently in response to local increases in neural activity – a process called functional hyperemia (Iadecola, 2017). These vascular dynamics underlie hemodynamic imaging techniques used to map regional neural activity, such as blood oxygenation level-dependent (BOLD) fMRI (Logothetis and Wandell, 2004; Vanzetta et al., 2004; Raichle and Mintun, 2006; Howarth et al., 2021). Arteriole dynamics are also crucial in buffering the brain from fluctuations in systemic blood pressure (autoregulation), and in driving clearance of metabolic waste products from the brain along perivascular spaces (Cipolla, 2009; Zhao et al., 2015; Iadecola, 2017; Presa et al., 2020; van Veluw et al., 2020; Rasmussen et al., 2021). Proper regulation of arteriole dynamics is essential to healthy brain function, as deterioration of neurovascular coupling, cerebral perfusion, and brain clearance contributes to the pathogenesis of many neurologic disorders (Gorelick et al., 2011; Iadecola, 2013; Snyder et al., 2015; Sweeney et al.,

2018; Rasmussen et al., 2021). Thus, there is widespread interest in understanding vascular dynamics and how neural activity interacts with and shapes hemodynamic responses.

In vivo studies of functional hyperemia typically engage vascular dynamics indirectly by activating neurons (for example with sensory stimulation), which in turn leads to the hemodynamic response. This makes it difficult to study intrinsic properties of the blood vessels, independent from neuronal activity and neurovascular coupling pathways. For instance, impaired vascular responses in disease may be due to reduced neural activity, altered neurovascular coupling, or loss of compliance in the vascular wall. Similarly, the kinetics of arterial contraction and relaxation *in vivo* cannot be understood independently of the kinetics of the neurovascular coupling mechanisms. The need to modulate arteriole diameter and/or blood flow independently from neural activation has led to the use of pharmacological approaches or systemic manipulations (such as a CO_2 challenge or system-wide changes in blood pressure) (Kara and Friedlander, 1999; Leithner et al., 2010; Tarantini et al., 2015; Masamoto and Vazquez, 2018). However, these methods do not provide spatiotemporal specificity. Intracortical injection of vasoactive substances improves spatial specificity (Cai et al., 2018), but remains low throughput and can act on non-vascular cell types. Due to these limitations, there is a need for methods to directly activate the microvasculature with high spatiotemporal resolution.

Recently, optogenetic techniques have been developed to control vessel diameter with light by expressing opsins in smooth muscle cells. Most studies to date have used wide-field activation of ChR2 with visible wavelength light. However, this technique affects vessels over a large region and predominantly activates the superficial vasculature, limiting the spatial resolution achieved (Wu et al., 2015; Zhang et al., 2015; Rorsman et al., 2018). Some studies have improved the spatial resolution of optogenetics by using visible wavelength lasers to create a focal point of activation, but this also activates primarily surface vessels (Hill et al., 2015; Mateo et al., 2017; Nelson et al., 2020). Achieving greater imaging depths has been attempted with fiber bundle probes (Kim et al., 2017) but this reduces imaging resolution and causes tissue damage. Two-photon optogenetic activation allows deeper imaging and more precise spatial control than single-photon activation. This method has been used to activate ChR2 in mural cells to examine contractility with single-vessel resolution (Hill et al., 2015; Tong et al.,

2020a; Hartmann et al., 2021). However, imaging and excitation in these studies required use of the same laser, limiting the ability to separate regions of stimulation from observation. Further, these studies used the original ChR2(H134R) variant, and opsins with improved two-photon cross sections have since become available.

Here, we introduce an approach to constrict cerebral arterioles with high spatiotemporal resolution up to hundreds of microns below the surface. We use the red-shifted opsin ReaChR (Lin et al., 2013) which has strong photocurrents and a long activation wavelength well-suited for two-photon stimulation. This method allows for constriction of individual or multiple branches of pial or penetrating arterioles by driving cell-specific depolarization of smooth muscle cells. By combining dual-light paths and independent focusing of the excitation and imaging lasers, we constricted vessels independently from the depth of the imaging plane, making this a useful tool to manipulate and monitor vessel diameter in three dimensions. This approach is advantageous over ChR2 activation of vascular smooth muscle because it can manipulate single vessels over larger cortical depths, and longer wavelengths of light are less likely to create spurious vascular changes independent of opsin expression (Rungta et al., 2017).

Results

ReaChR potently depolarizes cells when illuminated with red light (Lin et al., 2013), and exhibits peak two-photon activation efficiency at ~1000 nm (Chaigneau et al., 2016). This makes it ideal for combined two-photon activation and imaging of cerebrovasculature, similar to the all-optical methods developed to activate neurons *in vivo* using long-wavelength light (~1040 nm) while simultaneously imaging with shorter-wavelengths (~800–950 nm) (Packer et al., 2015; Carrillo-Reid et al., 2016; Shemesh et al., 2017; Mardinly et al., 2018; Marshel et al., 2019). To selectively express ReaChR in mural cells, we crossed ReaChR reporter mice with PDGFRβ-Cre mice (see Methods; **Figure 1A**), which allows expression of ReaChR tagged with mCitrine in vascular smooth muscle cells and pericytes, with negligible off-target expression in neurons or astrocytes (Hartmann et al., 2015)(**Figure 1B**). We imaged vasoconstrictive responses with two-photon microscopy while depolarizing the vascular mural cells either with a high power, pulsed 1040 nm laser or using a 594 nm light-emitting diode (LED) for single-photon activation (**Figure 1C**).

Single-photon activation of ReaChR in vessel walls produces widespread vasoconstriction

We first examined ReaChR activation with single-photon stimulation using a 594 nm LED to stimulate vessels broadly across the cranial window. We found that a single 100 ms pulse of light led to the rapid and widespread constriction of pial arterioles, which then relaxed back to baseline values within 30 seconds of activation (**Figure 2A-D; Movie 1**). In addition to the arteriole constriction, we also observed a weaker constriction (~2-3%) in the pial veins (**Figure 2A-D**). Although some expression of the opsin was seen in venous mural cells (**Figure 1B**), the venous response was likely a passive deflation due to widespread reduction in blood flow caused by arteriole constriction (Masamoto and Vazquez, 2018). This is because venous constriction was slower than the arteriole constriction, with the time to 25% constriction (1.2 seconds) and maximal constriction (5.2 seconds) delayed relative to arterioles (0.6 and 3.3 seconds respectively). Additionally, targeted two-photon activation (described below) produced large constrictions in arterioles but not veins (**Figure 2-1**).

We also observed that penetrating arterioles at least 300 μm deep in the cortex constricted with single-photon activation (**Figure 2E-G, Movie 2**). When we applied repeated trains of 100 ms pulses, we were able to sustain penetrating arteriole constriction at 10-20% below baseline levels for over a minute while simultaneously imaging in between each pulse train (**Figure 2H-I and Movie 3**). To demonstrate that constricted arterioles reduced downstream microvascular flow, we performed a line scan on a penetrating arteriole and a first order branch 85 μm deep in the tissue, which provides a measure of blood outflow to the capillary bed (**Figure 3**). The number of red blood cells (seen as dark streaks in the line scan) was greatly reduced in the branch within one second of stimulation and flow completely stopped for approximately 2 seconds before returning to normal by 6.5 seconds post-stimulation (**Figure 3B**). The penetrating arteriole rapidly constricted and the flow also stopped briefly around 2 seconds post-stimulation (**Figure 3B**). Altogether, these results show that single photon activation of ReaChR in smooth muscle cells causes rapid and robust vasoconstriction and reduced blood flow to the parenchyma.

Two-photon activation of ReaChR-expressing mural cells produces focal vasoconstrictions

120 Two-photon light provides greater spatial resolution and targeting of deeper vessels compared
121 to the single-photon activation achieved with the LED. To investigate the spatial control
122 achievable with two-photon optogenetic activation of arterioles, we used a spatial light
123 modulator (SLM) (Chen et al., 2018; Yang and Yuste, 2018) to split a single 1040 nm
124 stimulation beam into multiple beamlets that could be focused on specific locations of interest.
125 With this method, vasoconstriction was only observed when the stimulation spots were
126 contacting the vessel wall (**Figure 4A-E**). No vasoconstriction was observed when the edges
127 of the stimulation spots were 10 μm from the vessel wall, indicating high spatial precision in the
128 X-Y plane. Stimulating pial arterioles led to robust constrictions that were constrained to a few
129 tens of microns around the stimulation spots. We were able to constrict two neighboring
130 branches of a pial arteriole, separated by ~100 μm, independently with no overlap of
131 constrictive responses (**Figure 4F-I, Movies 4&5**).

132 Two-photon stimulation also allows targeting of individual vessels deeper in the cortex. We
133 imaged a region with two penetrating arterioles 200 μm below the cortical surface. By splitting
134 the stimulation beam and positioning spots over each vessel, we were able to constrict each
135 vessel independently of the other (**Figure 4J-M**), showing precise control of vascular diameter
136 between neighboring penetrating arterioles.

137 **Minimal spread of constriction along pial arterioles regardless of laser power**

138 We next assessed the spatial precision of constriction along the length of the vessel. The
139 difference images in **Figures 4B-C, G-H** demonstrated that there was very limited spread of
140 the constriction beyond the stimulation spots. We tested the effect of laser power on the spatial
141 spread of constriction by stimulating with a broad range of power levels. We found that
142 increasing the laser power led to a small increase in the spread of constriction. For example, a
143 30-fold increase in power (from 5 mW to 150 mW total power) led to ~3-fold increase in spread
144 of constriction (from 25 μm away from the center of stimulation to 75 μm) (**Figure 5A-H**).
145 Increasing the power to ~230 mW led to damage of the vessel wall. Although the threshold for
146 damage varied depending on vessel size and the number and arrangement of the stimulation
147 spots, we consistently observed that high powers (typically > 200 mW total across 4-6 spots)
148 on pial arterioles caused i.v. dye extravasation, and this was occasionally accompanied by
149 widespread vasoconstriction (**Movie 6**). Laser-induced vascular injury was also observed at

very high powers (> 250 mW) in control mice expressing only YFP in mural cells (see **Movies 7-8**). However, at the lower laser powers routinely used to induce vasoconstriction in ReaChR mice, we did not observe constrictions in control mice (**Figure 5-1**, **Movies 9-10**). This confirms that the focal constrictions we see at lower laser powers are ReaChR-dependent and not attributable to direct effects of light on blood vessels (Rungta et al., 2017; Rorsman et al., 2018).

Stimulation power influences the axial resolution of photoactivation

The precision of two-photon photoactivation in 3-D also depends on the resolution in the axial dimension, where the point-spread-function is larger than in the lateral dimension (Rickgauer and Tank, 2009; Packer et al., 2015). To measure the axial resolution, we used the SLM to position stimulation spots at multiple depth planes above and below a pial arteriole while imaging the center of the arteriole (**Figure 6A-B**). When spots were focused 100 μm above or below the vessel at 115 mW total power, there was still approximately 25-35% of the constriction seen when stimulating in the same plane as the vessel. At 150 μm below the vessel, constriction had dropped to ~10% (**Figure 6C-D**). Constriction was greater when the stimulation was above the pial surface than when it was deeper in the tissue, likely due to increased light scattering when penetrating the cortical tissue (**Figure 6D** – compare “above pia” with ‘parenchyma”).

To ensure that the SLM was accurately focusing the laser power throughout the depth range, we bleached a fluorescent slide with SLM stimulation at the imaging plane and 200 μm above and below the imaging plane. This confirmed that the region of excitation was accurately shaped and placed regardless of the SLM focal plane (**Figure 6-1A-B**).

Next, we tested the effect of laser power on the axial range of constriction. While the higher laser power used in **Figure 6C-D** showed substantial axial spread, pial vessels can be constricted with much lower power levels (**Figure 5**). When lower laser powers were used (20-44 mW), we found that arterial constriction was almost exclusively restricted to the stimulation plane, although the magnitude of the constrictive response was reduced (**Figure 6E**).

An important consideration in determining out-of-focal-plane activation, is that the cone of light extends laterally outside of the focal plane. This could lead to a greater lateral spread of

activation outside the focal plane than seen within the plane in **Figure 4E**. Therefore, we repeated the lateral resolution test with high laser power (115 mW) at different depth planes. We found that when the stimulation spots were laterally offset from the vessel wall, vasoconstriction was greater 50-150 μm below the imaging plane than at the imaging plane. However, just a 10 μm lateral offset resulted in very small vasoconstriction at all depths except when very high power levels were used (200 mW) (**Figure 6F**).

Thus, for precise 3D targeting of vasoconstriction, care must be taken in the experimental design to avoid unwanted activation of vessels located within the light cone but outside the focal plane. The range of out-of-focus activation will depend not only on the laser power applied, but also on the objective used, the orientation of the vessel relative to the light cone, and the size of the arteriole.

Vasoconstriction in the axial plane along penetrating arterioles

We next measured the spread of constriction in the axial plane through penetrating arterioles. We stimulated penetrating arterioles 200 μm below the surface with a range of powers and imaged in the stimulation plane and 150-175 μm superficial to that plane (**Figure 7A-C**). We found that low powers (20-30 mW) could constrict penetrating arterioles in the stimulation plane with little spread to the superficial plane. With higher powers, (~70 mW), near maximal constriction could be achieved but this led to ~50% maximal constriction in the superficial plane. And with much higher power (>150 mW), near maximal constriction could be achieved in both planes. Since penetrating arterioles supply columns of cortical microvasculature (Shih et al., 2013), the use of high powers to constrict a large span of the penetrating arteriole could be useful for modulating blood flow to a column of cortical tissue in a reversible manner (**Figure 7-1**).

Optogenetic vasoconstriction is slower and smaller in microvessels

Previous work has shown that prolonged optogenetic stimulation of pericytes expressing ChR2 leads to slow constriction of capillaries (Nelson et al., 2020; Hartmann et al., 2021). We therefore tested the efficacy of ReaChR for optogenetic constriction of pericytes. We divided vessels into three categories: Penetrating arterioles (covered by α-SMA-positive SMCs), arteriole-capillary transitional vessels (branch orders 1-4; covered by α-SMA-positive

ensheathing pericytes) and capillaries (branch orders 5-9; covered by α-SMA-low/negative capillary pericytes)(**Figure 8A**)(Hartmann et al., 2021). Brief pulses of single-photon excitation with the 594 nm LED led to ~14% constriction of penetrating arterioles, ~5% constriction of transitional vessels and a small ~1% constriction of capillaries (**Figure 8B**). Single pulses of two-photon stimulation, which elicited robust constriction in penetrating arterioles, led to minimal (~1%) constriction of transitional vessels and no constriction in capillaries (**Figure 8C**). To determine if more prolonged stimulation of ReaChR would induce constriction, we applied repeated pulses of light with the SLM for 40 seconds (**Figure 8D**). While transitional vessels constricted by ~3-4%, capillaries still showed negligible constriction. We then considered the duty cycle of stimulation. Our prior studies stimulated pericytes using line-scanning for near constant laser stimulation (Hartmann et al., 2021), whereas the SLM pulses used here were 100 ms with 0.5-1.5 seconds between pulses. Continuous line-scan stimulation at 1045 nm led to rapid constriction in penetrating arterioles and slower constrictions in the other vessel categories (**Figure 8E**). Consistent with our prior findings (Hartmann et al., 2021), capillaries exhibited a gradual constriction over 60 seconds of stimulation. Transitional vessels exhibited a more rapid constriction in the early phase. Constriction of both capillaries and transitional vessels reached a maximum of ~10% (**Figure 8D**). These results show that near continuous stimulation provided by line-scans is necessary to constrict the smallest microvessels.

Faster vasoconstriction with mural cell activation of ReaChR compared to ChR2

We next compared the contractile kinetics of mural cells expressing ReaChR with our previous data from mice expressing ChR2 in mural cells (Hartmann et al., 2021)(**Figure 9A,B**). We computed the rate of constriction over the first 10 seconds of stimulation for capillaries and transitional vessels (**Figure 9C**). Penetrating arterioles expressing ReaChR constricted rapidly and had nearly plateaued in their response by 10 seconds, so we computed the rate of constriction for the first 5 seconds of stimulation for the penetrating arterioles (**Figure 9C**). Capillaries showed similar, slow contractile dynamics, but transitional vessels and penetrating arterioles exhibited more rapid initial constriction with ReaChR compared to ChR2 vessels.

Optogenetic vasoconstriction is attainable in awake animals

To ensure that vessels could also be precisely targeted in awake animals, we replicated some key findings in awake mice. As in the anesthetized animals, brief pulses of light from the LED

238 evoked rapid robust constrictions and the constrictions could be maintained with repeated light
239 pulses (**Figure 10A-B**). Additionally, two-photon activation provided single-vessel precision of
240 vasoconstriction (**Figure 10C)**. In general, there was a slight decrease in constriction
241 amplitude and faster return-to-baseline in awake versus anesthetized animals.

242 **Use of optogenetic stimulation to modulate sensory-evoked dilation**

243 We next examined the utility of this technique to directly modulate the physiological dynamics
244 of brain arterioles, thereby providing a novel means to dissociate vascular and neuronal
245 responses in complex processes, such as functional hyperemia and vasomotion. Modulation of
246 physiological dynamics is possible because optogenetic activation of mural cells evokes rapid
247 contraction within hundreds of milliseconds (**Figure 11-1**), compared to the slower dynamics of
248 neurovascular coupling, which occurs on the order of seconds (Silva et al., 2000; Hillman,
249 2014). We directly compared the response latency of optogenetically-evoked constriction to
250 visually-evoked dilation in the same penetrating arterioles, and found, as expected, much
251 faster responses to the optogenetic stimulation (0.6 seconds to reach 25% of peak response)
252 than to the visual stimulus (3.4 seconds to 25% peak dilation; **Figure 11A – magenta vs.**
253 **blue**).

254 As a proof-of-principle experiment, we determined whether optogenetically-driven constriction
255 could alter sensory-evoked vasodilation. We presented 5 seconds of visual stimulation
256 together with a brief 100 ms pulse of optogenetic stimulation. This led to a rapid constriction of
257 the vessel followed by a dilation that was lower in amplitude than the dilation to the sensory
258 stimulus alone (**Figure 11A-B green vs. blue**). By reducing the visual stimulus duration from
259 5 seconds to 2 seconds, the same light pulse completely suppressed the dilation phase of the
260 vascular response following the initial rapid constriction (**Figure 11A-B, red vs. blue**).
261 Similarly, using multiple pulses of light during the visual stimulation was also sufficient to
262 eliminate the sensory-evoked vasodilation, as shown in population data across animals
263 (**Figure 11-2**). Thus, vasodilation to a sensory stimulus can be negated by optogenetic
264 "clamping" of arteriole diameter.

265

266 **<u>Discussion</u>**

267 Building on techniques recently developed for all-optical interrogation of neurons (Packer et al.,
268 2015; Carrillo-Reid et al., 2016; Marshel et al., 2019), we introduce a technique for all-optical
269 interrogation of the brain vasculature. We expressed the red-shifted opsin ReaChR in vascular
270 mural cells to control blood flow rapidly and reversibly over a range of spatiotemporal scales *in*
271 *vivo*. Single-photon activation produced widespread vasoconstriction across the full cranial
272 window, whereas two-photon activation provided single-vessel control of constriction in 3-D.
273 Single brief pulses of light could produce robust vasoconstriction with rapid onset, and
274 repeated light pulses could maintain prolonged constriction. Optical stimulation of mural cells
275 expressing ReaChR is therefore a powerful approach for studying arteriole vasoconstriction,
276 and for dissociating neuronal and vascular activity in complex processes such as
277 neurovascular coupling and vasomotion.

278 Prior studies have utilized the original variant of channelrhodopsin, ChR2 (H134R), to achieve
279 vasoconstriction in vascular mural cells *in vivo*. One- and two-photon activation of ChR2 led to
280 the gradual constriction of arterioles, requiring >20 seconds to reach a minimum diameter with
281 near-constant activation (Hill et al., 2015; Tong et al., 2020a; Hartmann et al., 2021). In
282 contrast, continuous activation of ReaChR in penetrating arterioles (using laser line-scanning)
283 led to a more rapid constriction, reaching a minimum in <15 seconds, that was greater in
284 amplitude and returned to baseline more quickly. This suggests that ReaChR is superior to
285 ChR2 for two-photon optogenetic studies of the vasculature, likely because of the higher
286 photocurrent amplitude in ReaChR, compared to ChR2 (H134R), at their respective optimum
287 excitation wavelengths (Lin et al., 2013). The improved tissue penetration of 1040 nm light
288 used to activate ReaChR may also increase stimulation efficiency for parenchymal vessels
289 (Chaigneau et al., 2016).

290 ReaChR is among the most potent red-shifted opsins for two-photon activation as shown in
291 neurons (Chen et al., 2019), and its availability as a floxed mouse line allows vascular
292 targeting experiments. Mural cells are not easily transduced *in vivo* using viral approaches. An
293 additional advantage is that the optimal activation wavelength of ReaChR (>1000 nm) does not
294 substantially interfere with imaging of common fluorophores, whereas two-photon ChR2
295 activation can occurs around the imaging wavelengths used for calcium indicators such as

296 Oregon Green or GCaMP (Prakash et al., 2012). This feature facilitates independent imaging
297 or neural activity and vascular stimulation with separate laser lines.

298 The highly localized constriction we see following a focal activation differs from vasodilation
299 responses seen during functional hyperemia. Following focal activation of neural tissue,
300 vasodilatory signals propagate several millimeters from the activation site (Iadecola et al.,
301 1997; Chen et al., 2011). This long-range propagation of dilation is attributed to endothelial cell
302 signaling through gap junctions (Chen et al., 2014; Longden et al., 2017; Zechariah et al.,
303 2020), and influences the spatial precision of vascular imaging (e.g. fMRI) signals (O'Herron et
304 al., 2016; Rungta et al., 2018; Drew, 2019). The lack of propagation seen when directly
305 activating smooth muscle cells supports the notion that endothelial rather than smooth muscle
306 cells mediate the long-range propagation of signals through vessel walls. However, differences
307 in the propagation characteristics of hyperpolarizing (dilatory) versus depolarizing (constrictive)
308 signals along the vascular wall may also play a role in the propagation range of the signals.

309 We anticipate that this technique will be useful for studies requiring assessment of vascular
310 dynamics *in vivo*. The ability to directly modulate vessel diameter and blood flow levels with
311 high spatiotemporal precision could be useful for understanding vascular wall kinetics. We
312 have shown that it is possible to study the contractile kinetics of different vessel types within
313 the microvascular network. Our data confirms the distinct kinetics across arterioles,
314 transitional, capillary and venous zones, with slow contraction occurring in capillaries covered
315 by αSMA-negative/low pericytes. These slow kinetics have implications for how capillary
316 pericytes contribute to blood flow regulation, which is likely more relevant slow aspects of
317 functional hyperemia and maintenance of basal capillary flow and flow heterogeneity
318 (Hartmann et al., 2021; Berthiaume et al., 2022; Hartmann et al., 2022).

319 The ability to concurrently monitoring neural and/or astrocytic activity alongside vessels during
320 vascular manipulation opens additional opportunities to study questions on neuro-glia-vascular
321 coupling. For example, offsetting stimulus evoked dilations (**Figure 11**) while monitoring neural
322 activity can shed light on how neuronal function depends on functional hyperemia (Moore and
323 Cao, 2008) Neural circuits are extremely complex with many different sub-types of neurons
324 playing different roles. These subtypes have been shown to have different metabolic
325 sensitivities and thus, may be differentially affected by blocking functional hyperemia (Kann,

326 2016). This could lead to altered circuit activity which could have profound consequences for
327 neural processing. Additionally, the energy budgets of different cellular functions within
328 neurons are quite different (Howarth et al., 2012) and reducing available energy by blocking
329 functional hyperemia could lead to differing degrees of dysfunction across important cellular
330 processes (e.g. re-establishing the membrane potential, recycling neurotransmitters) which
331 could again have important consequences for neural coding. Furthermore, it has been shown
332 that there is a steep gradient of oxygen moving away from penetrating arterioles and neurons
333 at greater distances from vessels may be differentially affected by blocking the hyperemic
334 response (Devor et al., 2011).

335 Optical control of arteriole tone can also be used to study "vasculo-neuronal coupling", a
336 process where alteration in vessel tone modifies neural and astrocyte signals. Theoretical
337 (Moore and Cao, 2008) and brain slice (Kim et al., 2016) studies have proposed the existence
338 of such processes. With our technique, detailed *in vivo* investigations with vascular
339 optogenetics are now possible to fully dissect neuron-vessel interactions. In addition, the role
340 of vasomotion in clearance of metabolic waste through perivascular pathways also requires
341 new approaches to directly drive the diameter of arterioles *in vivo* (van Veluw et al., 2020). For
342 example, it provides tools to examine whether augmentation of vasomotion can reduce brain
343 pathology in models that involve accrual of metabolic waste products in brain tissue.

344 Impaired functional hyperemia is seen in numerous neurologic diseases, including acute
345 injuries caused by ischemia (Summers et al., 2017), and during progressive, age-related
346 pathologies such as cerebral amyloid angiopathy and other small vessel diseases (Niwa et al.,
347 2002; Park et al., 2014). It is currently hard to dissect the basis of impaired neurovascular
348 responses, as defects could arise from loss of neuronal activation, vascular reactivity, coupling
349 between these two processes, or a combination thereof. Vascular specific changes can be
350 assessed *ex vivo* in isolated vessels (Tong and Hamel, 2015). However, traditional *in vivo*
351 approaches rely on driving of sensory input by engaging neurons first, or use of non-specific
352 vasodilatory stimuli (hypercapnia, isoflurane, pharmacology) with complex effects on all
353 components involved. The ability to selectively block the vascular response with optogenetics
354 provides cleaner access for probing neurovascular physiology *in vivo*, independent of neural
355 activity.

356

357 **Materials and Methods**

358 Experiments were performed at the Medical University of South Carolina (MUSC) and Augusta
359 University (AU). All surgical and experimental procedures were approved by the Institutional
360 Animal Care and Use Committees of the Universities.

361 **Animals:** Mice were generated at our Institutions by crossing heterozygous PDGFRβ-Cre
362 male mice (courtesy of Dr. Volkhard Lindner, Maine Medical Center Research Institute) with
363 heterozygous female opsin mice (floxed ReaChR-mCitrine; Jackson Laboratories: Strain
364 #026294). Control mice were generated by crossing the same PDGFRβ-Cre males with Ai3
365 females (floxed YFP; Jackson Laboratories: Strain #007903). Bigenic progeny from these
366 crosses displayed green fluorescence in the vasculature under blue illumination in tail snips or
367 ear punches. Male and female mice were used aged 2-12 months.

368 **Surgeries:** Mice were anesthetized with a bolus infusion of fentanyl citrate (0.04–0.05 mg kg^{-}
369 ^{1}), midazolam (4–5 mg kg^{-1}), and dexmedetomidine (0.20–0.25 mg kg^{-1}) several hours after an
370 intramuscular injection (0.03 mL) of dexamethasone sodium phosphate (4 mg mL^{-1}). The heart
371 and respiration rates of the animals were continually monitored throughout the surgeries using
372 pulse oximetry (PhysioSuite, Kent Scientific). The scalp was excised, the skull cleaned, and a
373 custom-made head-plate was fixed to the skull with C&B MetaBond quick adhesive cement
374 (Parkell; S380). Craniotomies (2–3 mm) were opened over the primary visual cortex centered
375 approximately 2.5 mm lateral to the lambda suture and 1-1.5 mm anterior to the transverse
376 sinus. Craniotomies were sealed with a glass coverslip consisting of a round 3 mm glass
377 coverslip (Warner Instruments; 64-0720 (CS-3R)) glued to a round 4 mm coverslip (Warner
378 Instruments; 64-0724 (CS-4R)) with UV-cured optical glue (Norland Products; 7110). The
379 coverslip was positioned with the 3 mm side placed directly over the cortical surface, while the
380 4 mm coverslip laid on the skull at the edges of the craniotomy. An instant adhesive (Loctite
381 Instant Adhesive 495) was carefully dispensed along the edge of the 4 mm coverslip to secure
382 it to the skull, taking care not to allow any spillover onto the brain. Lastly, the area around the
383 cranial window was sealed with dental cement. Animals were given at least 3 weeks to recover
384 and to ensure the window would be optically clear before imaging took place.

385 **Animal imaging:** During imaging sessions, mice were anesthetized with ~30 μL
386 chlorprothixene (1 mg/mL, intramuscular) and low levels of isoflurane (≤ 0.8%). Heart rate and
387 respiration rate were continuously monitored to ensure consistent anesthetic depth and
388 animals were kept on a heating pad to maintain body temperature. Either fluorescein
389 isothiocyanate (FITC) dextran (MW = 2000 kDa) or Texas Red (70 kDa) dextran (5% w/v in
390 saline) was injected retro-orbitally (20-40 μL) under an initial high level of isoflurane (>2%).
391 When visual stimuli were presented, the injections were in the eye not being stimulated by the
392 computer display monitor. Isoflurane levels were returned to ≤ 0.8% for at least 15 minutes
393 before data collection began.

394 **Awake imaging**: Animals were gradually acclimated to awake head restraint on a treadmill
395 allowing for voluntary locomotion. Imaging experiments were conducted following a minimum
396 of two weeks of training. Animals were briefly anesthetized with >2% isoflurane while the retro-
397 orbital injection of the vascular dye was performed. We then allowed 15 minutes to recover
398 before beginning the imaging.

399 **Equipment:** Imaging data was collected using the Ultima 2P-Plus two-photon microscope
400 system (Bruker Corporation – see **Figure 1C**). At MUSC we used a beta version of the Ultima
401 2P-Plus. The major differences from the full version at AU were that the beta version did not
402 have the 594 nm LED for single-photon stimulation or the Electro-Tunable Lens (ETL). At
403 MUSC, an Insight X2 (Spectra-Physics, MKS Instruments Inc.) was used for imaging and a
404 FemtoTrain (Spectra-Physics: 1040 nm, ~3.5W average power; < 370 fs pulse width; > 350 nJ
405 pulse energy) was used for optogenetic stimulation. At AU we used the tunable line from the
406 Insight X3 (Spectra-Physics) for imaging and the fixed 1045 nm line (~4W average power;
407 <170 fs pulse width; ~44 nJ pulse energy) from the same laser for stimulation. Dedicated fixed
408 wavelength lasers used for two-photon optogenetics typically have lower repetition rates and
409 higher pulse powers than imaging lasers like the Insight X3. Nevertheless, despite the lower
410 pulse energy, the fixed line from the Insight X3 was sufficient to evoke constrictions – even
411 deep in the cortex. No differences were observed in the results obtained at the two institutions
412 and so results were combined.

413 Pockels Cells (350-80, Conoptics) were used to control laser power. The stimulation beam was
414 passed through a Spatial Light Modulator (SLM, HSP512-1064, Meadowlark Optics) to create

415 three-dimensional activation patterns. A dichroic mirror (reflectance band from 1010-1070 nm)
416 combined the two lasers downstream of the galvanometer mirrors. Imaging was performed
417 using Nikon objectives (CFI75 LWD 16X W and CFI75 Apochromat 25XC W 1300).

418 Because of the intensity of the stimulation light (for both single- and two-photon illumination)
419 and the potential for extremely bright fluorescence from excitation via the stimulation laser, the
420 PMT detectors were fitted with fast mechanical shutters which block incoming light during the
421 optical stimulation periods. This is seen in all the movies as a brief dimming of the image when
422 the stimulation light is on. Our strategy was to use brief stimulation intervals at low repetition
423 rates to allow sufficient data on arteriole diameter to be measured between stimulus pulses.

424 The LED on the Ultima 2P-Plus was positioned in the light path on the collection side of the
425 primary dichroic (**Figure 1C**). To send this light to the objective, a cube was positioned in the
426 path between the PMT and the objective containing both a mirror that reflects a band of light
427 around the LED wavelength (570-605 nm) and a filter that blocks red light from reaching the
428 PMT detectors (near-zero transmission band from 575-605 nm). This resulted in a modest
429 reduction of the Texas Red signal in this mode.

430 **Optical Stimulation: A. Single-photon.** For single-photon stimulation, we used a 594 nm
431 LED. We used 100 ms pulses of light. When a train of pulses was given, there were 100 ms
432 between pulses. Details of the pulse timing are given in the figure legends.

433 **B. Two-photon.** For two-photon stimulation, we used the SLM to split the stimulation laser
434 beam into multiple spots (or beamlets). Each stimulation spot was spiraled over a small region
435 (12-25 μm, 5 revolutions, one time per light pulse, see **Figure 2-1D**) using the galvanometer
436 mirrors to increase the area of activation (Packer et al., 2015; Carrillo-Reid et al., 2016). Single
437 100 ms pulses were typically used. Laser powers were typically 50-200 mW per vessel, spread
438 over 4-6 spots for pial arterioles and 2-3 spots for penetrating arterioles. Although higher
439 powers led to damage of vessel walls and dye leakage on the surface in pial arterioles, even
440 the highest powers we used (>300 mW per vessel) in penetrating arterioles caused no visible
441 damage or leakage. To determine the power of the stimulation spots, we used a power meter
442 while presenting random patterns of 4 and 6 spots. It is not feasible to calibrate the power in
443 each spot separately so we divided the overall power by the number of spots to obtain an
444 estimate of the power of each spot. The total power varied somewhat (typically <10%) from

445 pattern to pattern and the amount of power each spot receives depends on its position on the
446 SLM (Mardinly et al., 2018). Since it was not possible to know what spot pattern was required
447 until we were positioning them on the vessels, the exact power applied to each vessel in each
448 experiment is an estimate.

449 **Optical Imaging:** Images were usually collected using resonant scanning mode at 3.75
450 frames/second, except for **Figure 11-1** (15 frames/second). Vessels were imaged at 875 nm
451 when labeled with Texas Red dextran and 800 nm when imaged with FITC dextran.

452 Although 920 nm is in the tail of the activation spectrum for red-shifted opsins like ReaChR
453 (Chaigneau et al., 2016), wavelengths in this range are typically used in all-optical (activation
454 and imaging) neural approaches (Packer et al., 2015; Carrillo-Reid et al., 2016; Marshel et al.,
455 2019). These previous studies reported that low laser powers for imaging prevents photo-
456 activation from the imaging laser. We typically imaged Texas Red at 875 nm and saw no
457 evidence that the imaging laser led to vasoconstriction. When we imaged at 920 nm, we did
458 see slight constrictions in pial arterioles with moderate power levels (>20 mW), but under
459 normal conditions, the vascular dye was sufficiently bright to reduce imaging power below
460 these levels and eliminate constriction caused by the imaging laser. The possibility of
461 constriction due to the imaging laser is important to keep in mind when choosing an
462 opsin/indicator combination. Although more sensitive opsins are usually desirable because
463 less light is needed to activate them and the stimulation beam can be split into more beamlets,
464 it will also make the cells more readily activated by the imaging laser.

465 It is also important to consider the effects of the emitted fluorescence on the opsin. Texas Red
466 emission overlaps the excitation peak for single-photon activation of ReaChR. This feature was
467 elegantly used in a recent study as a method for spatially precise single-photon excitation
468 (Tong et al., 2020b; Tong et al., 2020a). While we did not see evidence of a constant
469 constriction during imaging caused by the emission of Texas Red (further constriction was
470 always possible and vessels did not rapidly constrict at the start of an imaging run), the
471 constriction seen with higher imaging powers that we attributed to imaging laser activation may
472 have at least in part been caused by indirect actions of Texas Red emission on ReaChR.

473 **Visual Stimuli:** Drifting square-wave grating stimuli were presented on a 17-inch LCD monitor.
474 The gratings were presented at 100% contrast, 30 cd m^{-2} mean luminance, 1.5 Hz temporal

frequency, and 0.04 cycles/degree. The visual stimulus and the optogenetic pulses were both controlled by the imaging software, ensuring that the onset of both stimulation types were synchronized.

Data Analysis: Data were analyzed in Matlab (Mathworks) and ImageJ (National Institutes of Health). Blood vessel diameters were computed frame-by-frame using custom Matlab scripts (O'Herron et al., 2016; O'Herron et al., 2020). Diameters were normalized by the average of 15 frames prior to stimulation onset. Repetitions were aligned by the onset of the optical stimulation when averaged together. The latency of constriction (**Figure 11-1**) was computed using the Curve Fitting toolbox in Matlab. A two-phase equation was fit to the diameter time-course data (see (O'Herron and von der Heydt, 2011)), where phase one was a constant (the baseline diameter) and phase two was an exponential curve (following the constriction phase of the response). The fit is given by:

$$A \cdot \text{phase one}\ (t) + [A + C(\exp(-(t - t_1)/\tau) - C] \cdot \text{phase two}\ (t)$$

Where: $\text{phase one}\ (t) = \begin{Bmatrix} 1 \text{ for } t < t_1 \\ 0 \text{ else} \end{Bmatrix}$ and $\text{phase two}\ (t) = \begin{Bmatrix} 1 \text{ for } t_1 \leq t < 2 \text{ seconds} \\ 0 \text{ else} \end{Bmatrix}$

A is a constant representing the baseline value (nearly 0), C is the amplitude of the exponential and τ is its time constant. The time point where the fit switches between the two phases is the parameter t_1, which gives the onset latency. The data to fit are cut off at 2 seconds which was determined by eye to be near the rising phase of the response.

References:

Berthiaume A-A, Schmid F, Stamenkovic S, Coelho-Santos V, Nielson CD, Weber B, Majesky MW, Shih AY (2022) Deficiency in pericyte remodeling as a basis for impaired capillary flow and structure during brain aging. bioRxiv:2022.2004.2028.489881.

Cai C, Fordsmann JC, Jensen SH, Gesslein B, Lønstrup M, Hald BO, Zambach SA, Brodin B, Lauritzen MJ (2018) Stimulation-induced increases in cerebral blood flow and local capillary vasoconstriction depend on conducted vascular responses. Proc Natl Acad Sci U S A 115:E5796-e5804.

502 Carrillo-Reid L, Yang W, Bando Y, Peterka DS, Yuste R (2016) Imprinting and recalling cortical ensembles. Science
503 353:691-694.
504 Chaigneau E, Ronzitti E, Gajowa MA, Soler-Llavina GJ, Tanese D, Brureau AY, Papagiakoumou E, Zeng H, Emiliani
505 V (2016) Two-Photon Holographic Stimulation of ReaChR. Front Cell Neurosci 10:234.
506 Chen BR, Bouchard MB, McCaslin AFH, Burgess SA, Hillman EMC (2011) High-speed vascular dynamics of the
507 hemodynamic response. NeuroImage 54:1021-1030.
508 Chen BR, Kozberg MG, Bouchard MB, Shaik MA, Hillman EMC (2014) A Critical Role for the Vascular Endothelium
509 in Functional Neurovascular Coupling in the Brain. Journal of the American Heart Association 3.
510 Chen IW, Papagiakoumou E, Emiliani V (2018) Towards circuit optogenetics. Curr Opin Neurobiol 50:179-189.
511 Chen IW, Ronzitti E, Lee BR, Daigle TL, Dalkara D, Zeng H, Emiliani V, Papagiakoumou E (2019) In Vivo
512 Submillisecond Two-Photon Optogenetics with Temporally Focused Patterned Light. J Neurosci 39:3484-
513 3497.
514 Cipolla MJ (2009) Integrated Systems Physiology: From Molecule to Function. In: The Cerebral Circulation. San
515 Rafael (CA): Morgan & Claypool Life Sciences Copyright © 2010 by Morgan & Claypool Life Sciences.
516 Clark D, Sokoloff L (1999) In GJ Siegel, BW Agranoff, RW Albers, SK Fisher, & MD Uhler (Eds.), Basic
517 neurochemistry: Molecular, cellular and medical aspects (pp. 637–670). In: Philadelphia: Lippincott.
518 Devor A, Sakadžić S, Saisan PA, Yaseen MA, Roussakis E, Srinivasan VJ, Vinogradov SA, Rosen BR, Buxton RB, Dale
519 AM, Boas DA (2011) “Overshoot” of O2 Is Required to Maintain Baseline Tissue Oxygenation at Locations
520 Distal to Blood Vessels. The Journal of Neuroscience 31:13676-13681.
521 Drew PJ (2019) Vascular and neural basis of the BOLD signal. Curr Opin Neurobiol 58:61-69.
522 Gorelick PB et al. (2011) Vascular contributions to cognitive impairment and dementia: a statement for
523 healthcare professionals from the american heart association/american stroke association. Stroke
524 42:2672-2713.
525 Hartmann DA, Coelho-Santos V, Shih AY (2022) Pericyte Control of Blood Flow Across Microvascular Zones in the
526 Central Nervous System. Annu Rev Physiol 84:331-354.
527 Hartmann DA, Underly RG, Grant RI, Watson AN, Lindner V, Shih AY (2015) Pericyte structure and distribution in
528 the cerebral cortex revealed by high-resolution imaging of transgenic mice. Neurophotonics 2:041402.
529 Hartmann DA, Berthiaume AA, Grant RI, Harrill SA, Koski T, Tieu T, McDowell KP, Faino AV, Kelly AL, Shih AY
530 (2021) Brain capillary pericytes exert a substantial but slow influence on blood flow. Nat Neurosci
531 24:633-645.

532 Hill RA, Tong L, Yuan P, Murikinati S, Gupta S, Grutzendler J (2015) Regional Blood Flow in the Normal and
533 Ischemic Brain Is Controlled by Arteriolar Smooth Muscle Cell Contractility and Not by Capillary
534 Pericytes. Neuron 87:95-110.
535 Hillman EMC (2014) Coupling Mechanism and Significance of the BOLD Signal: A Status Report. Annual Review of
536 Neuroscience 37:161-181.
537 Howarth C, Gleeson P, Attwell D (2012) Updated energy budgets for neural computation in the neocortex and
538 cerebellum. J Cereb Blood Flow Metab 32:1222-1232.
539 Howarth C, Mishra A, Hall CN (2021) More than just summed neuronal activity: how multiple cell types shape
540 the BOLD response. Philos Trans R Soc Lond B Biol Sci 376:20190630.
541 Iadecola C (2013) The pathobiology of vascular dementia. Neuron 80:844-866.
542 Iadecola C (2017) The Neurovascular Unit Coming of Age: A Journey through Neurovascular Coupling in Health
543 and Disease. Neuron 96:17-42.
544 Iadecola C, Yang G, Ebner TJ, Chen G (1997) Local and propagated vascular responses evoked by focal synaptic
545 activity in cerebellar cortex. J Neurophysiol 78:651-659.
546 Kann O (2016) The interneuron energy hypothesis: Implications for brain disease. Neurobiol Dis 90:75-85.
547 Kara P, Friedlander MJ (1999) Arginine Analogs Modify Signal Detection by Neurons in the Visual Cortex. The
548 Journal of Neuroscience 19:5528-5548.
549 Kim KJ, Ramiro Diaz J, Iddings JA, Filosa JA (2016) Vasculo-Neuronal Coupling: Retrograde Vascular
550 Communication to Brain Neurons. J Neurosci 36:12624-12639.
551 Kim M, Hong J, Kim J, Shin HJ (2017) Fiber bundle-based integrated platform for wide-field fluorescence imaging
552 and patterned optical stimulation for modulation of vasoconstriction in the deep brain of a living animal.
553 Biomed Opt Express 8:2781-2795.
554 Leithner C, Royl G, Offenhauser N, Füchtemeier M, Kohl-Bareis M, Villringer A, Dirnagl U, Lindauer U (2010)
555 Pharmacological uncoupling of activation induced increases in CBF and CMRO2. J Cereb Blood Flow
556 Metab 30:311-322.
557 Lin JY, Knutsen PM, Muller A, Kleinfeld D, Tsien RY (2013) ReaChR: a red-shifted variant of channelrhodopsin
558 enables deep transcranial optogenetic excitation. Nat Neurosci 16:1499-1508.
559 Logothetis NK, Wandell BA (2004) Interpreting the BOLD signal. Annu Rev Physiol 66:735-769.
560 Longden TA, Dabertrand F, Koide M, Gonzales AL, Tykocki NR, Brayden JE, Hill-Eubanks D, Nelson MT (2017)
561 Capillary K(+)-sensing initiates retrograde hyperpolarization to increase local cerebral blood flow. Nat
562 Neurosci 20:717-726.

563 Mardinly AR, Oldenburg IA, Pégard NC, Sridharan S, Lyall EH, Chesnov K, Brohawn SG, Waller L, Adesnik H (2018)
564 Precise multimodal optical control of neural ensemble activity. Nat Neurosci 21:881-893.
565 Marshel JH, Kim YS, Machado TA, Quirin S, Benson B, Kadmon J, Raja C, Chibukhchyan A, Ramakrishnan C, Inoue
566 M, Shane JC, McKnight DJ, Yoshizawa S, Kato HE, Ganguli S, Deisseroth K (2019) Cortical layer-specific
567 critical dynamics triggering perception. Science 365.
568 Masamoto K, Vazquez A (2018) Optical imaging and modulation of neurovascular responses. J Cereb Blood Flow
569 Metab 38:2057-2072.
570 Mateo C, Knutsen PM, Tsai PS, Shih AY, Kleinfeld D (2017) Entrainment of Arteriole Vasomotor Fluctuations by
571 Neural Activity Is a Basis of Blood-Oxygenation-Level-Dependent "Resting-State" Connectivity. Neuron
572 96:936-948.e933.
573 Moore CI, Cao R (2008) The hemo-neural hypothesis: on the role of blood flow in information processing.
574 Journal of Neurophysiology 99:2035-2047.
575 Nelson AR, Sagare MA, Wang Y, Kisler K, Zhao Z, Zlokovic BV (2020) Channelrhodopsin Excitation Contracts Brain
576 Pericytes and Reduces Blood Flow in the Aging Mouse Brain in vivo. Frontiers in Aging Neuroscience 12.
577 Niwa K, Kazama K, Younkin L, Younkin SG, Carlson GA, Iadecola C (2002) Cerebrovascular autoregulation is
578 profoundly impaired in mice overexpressing amyloid precursor protein. American journal of physiology
579 Heart and circulatory physiology 283:H315-323.
580 O'Herron P, von der Heydt R (2011) Representation of object continuity in the visual cortex. Journal of Vision 11.
581 O'Herron P, Summers PM, Shih AY, Kara P, Woodward JJ (2020) In vivo two-photon imaging of neuronal and
582 brain vascular responses in mice chronically exposed to ethanol. Alcohol 85:41-47.
583 O'Herron P, Chhatbar PY, Levy M, Shen Z, Schramm AE, Lu Z, Kara P (2016) Neural correlates of single-vessel
584 haemodynamic responses in vivo. Nature 534:378-382.
585 Packer AM, Russell LE, Dalgleish HWP, Häusser M (2015) Simultaneous all-optical manipulation and recording of
586 neural circuit activity with cellular resolution in vivo. Nature Methods 12:140-146.
587 Park L, Koizumi K, El Jamal S, Zhou P, Previti ML, Van Nostrand WE, Carlson G, Iadecola C (2014) Age-Dependent
588 Neurovascular Dysfunction and Damage in a Mouse Model of Cerebral Amyloid Angiopathy. Stroke; a
589 journal of cerebral circulation 45:1815-1821.
590 Prakash R, Yizhar O, Grewe B, Ramakrishnan C, Wang N, Goshen I, Packer AM, Peterka DS, Yuste R, Schnitzer MJ,
591 Deisseroth K (2012) Two-photon optogenetic toolbox for fast inhibition, excitation and bistable
592 modulation. Nat Methods 9:1171-1179.
593 Presa JL, Saravia F, Bagi Z, Filosa JA (2020) Vasculo-Neuronal Coupling and Neurovascular Coupling at the
594 Neurovascular Unit: Impact of Hypertension. Front Physiol 11:584135.

595 Raichle ME, Gusnard DA (2002) Appraising the brain's energy budget. Proc Natl Acad Sci U S A 99:10237-10239.
596 Raichle ME, Mintun MA (2006) Brain work and brain imaging. Annu Rev Neurosci 29:449-476.
597 Rasmussen MK, Mestre H, Nedergaard M (2021) Fluid Transport in the Brain. Physiol Rev.
598 Rickgauer JP, Tank DW (2009) Two-photon excitation of channelrhodopsin-2 at saturation. Proceedings of the
599 National Academy of Sciences 106:15025-15030.
600 Rorsman NJG, Ta CM, Garnett H, Swietach P, Tammaro P (2018) Defining the ionic mechanisms of optogenetic
601 control of vascular tone by channelrhodopsin-2. Br J Pharmacol 175:2028-2045.
602 Rungta RL, Chaigneau E, Osmanski BF, Charpak S (2018) Vascular Compartmentalization of Functional Hyperemia
603 from the Synapse to the Pia. Neuron 99:362-375.e364.
604 Rungta RL, Osmanski BF, Boido D, Tanter M, Charpak S (2017) Light controls cerebral blood flow in naive
605 animals. Nat Commun 8:14191.
606 Shemesh OA, Tanese D, Zampini V, Linghu C, Piatkevich K, Ronzitti E, Papagiakoumou E, Boyden ES, Emiliani V
607 (2017) Temporally precise single-cell-resolution optogenetics. Nat Neurosci 20:1796-1806.
608 Shih AY, Blinder P, Tsai PS, Friedman B, Stanley G, Lyden PD, Kleinfeld D (2013) The smallest stroke: occlusion of
609 one penetrating vessel leads to infarction and a cognitive deficit. Nat Neurosci 16:55-63.
610 Silva AC, Lee SP, Iadecola C, Kim SG (2000) Early temporal characteristics of cerebral blood flow and
611 deoxyhemoglobin changes during somatosensory stimulation. J Cereb Blood Flow Metab 20:201-206.
612 Snyder HM, Corriveau RA, Craft S, Faber JE, Greenberg SM, Knopman D, Lamb BT, Montine TJ, Nedergaard M,
613 Schaffer CB, Schneider JA, Wellington C, Wilcock DM, Zipfel GJ, Zlokovic B, Bain LJ, Bosetti F, Galis ZS,
614 Koroshetz W, Carrillo MC (2015) Vascular contributions to cognitive impairment and dementia including
615 Alzheimer's disease. Alzheimers Dement 11:710-717.
616 Summers PM, Hartmann DA, Hui ES, Nie X, Deardorff RL, McKinnon ET, Helpern JA, Jensen JH, Shih AY (2017)
617 Functional deficits induced by cortical microinfarcts. J Cereb Blood Flow Metab 37:3599-3614.
618 Sweeney MD, Kisler K, Montagne A, Toga AW, Zlokovic BV (2018) The role of brain vasculature in
619 neurodegenerative disorders. Nat Neurosci 21:1318-1331.
620 Tarantini S, Hertelendy P, Tucsek Z, Valcarcel-Ares MN, Smith N, Menyhart A, Farkas E, Hodges EL, Towner R,
621 Deak F, Sonntag WE, Csiszar A, Ungvari Z, Toth P (2015) Pharmacologically-Induced Neurovascular
622 Uncoupling is Associated with Cognitive Impairment in Mice. Journal of Cerebral Blood Flow &
623 Metabolism 35:1871-1881.
624 Tong L, Yuan P, Chen M, Chen F, Bewersdorf J, Zhou ZJ, Grutzendler J (2020a) Single cell in vivo brain optogenetic
625 stimulation by two-photon excitation fluorescence transfer. bioRxiv:2020.2006.2029.179077.

626 Tong L, Hill RA, Damisah EC, Murray KN, Yuan P, Bordey A, Grutzendler J (2020b) Imaging and optogenetic
627 modulation of vascular mural cells in the live brain. Nat Protoc.
628 Tong XK, Hamel E (2015) Simvastatin restored vascular reactivity, endothelial function and reduced string vessel
629 pathology in a mouse model of cerebrovascular disease. J Cereb Blood Flow Metab 35:512-520.
630 van Veluw SJ, Hou SS, Calvo-Rodriguez M, Arbel-Ornath M, Snyder AC, Frosch MP, Greenberg SM, Bacskai BJ
631 (2020) Vasomotion as a Driving Force for Paravascular Clearance in the Awake Mouse Brain. Neuron
632 105:549-561.e545.
633 Vanzetta I, Slovin H, Omer DB, Grinvald A (2004) Columnar resolution of blood volume and oximetry functional
634 maps in the behaving monkey; implications for FMRI. Neuron 42:843-854.
635 Wu Y, Li SS, Jin X, Cui N, Zhang S, Jiang C (2015) Optogenetic approach for functional assays of the cardiovascular
636 system by light activation of the vascular smooth muscle. Vascul Pharmacol 71:192-200.
637 Yang W, Yuste R (2018) Holographic imaging and photostimulation of neural activity. Curr Opin Neurobiol
638 50:211-221.
639 Zechariah A, Tran CHT, Hald BO, Sandow SL, Sancho M, Kim MSM, Fabris S, Tuor UI, Gordon GRJ, Welsh DG
640 (2020) Intercellular Conduction Optimizes Arterial Network Function and Conserves Blood Flow
641 Homeostasis During Cerebrovascular Challenges. Arterioscler Thromb Vasc Biol 40:733-750.
642 Zhang S, Cui N, Wu Y, Zhong W, Johnson CM, Jiang C (2015) Optogenetic intervention to the vascular
643 endothelium. Vascul Pharmacol 74:122-129.
644 Zhao Z, Nelson AR, Betsholtz C, Zlokovic BV (2015) Establishment and Dysfunction of the Blood-Brain Barrier. Cell
645 163:1064-1078.

646

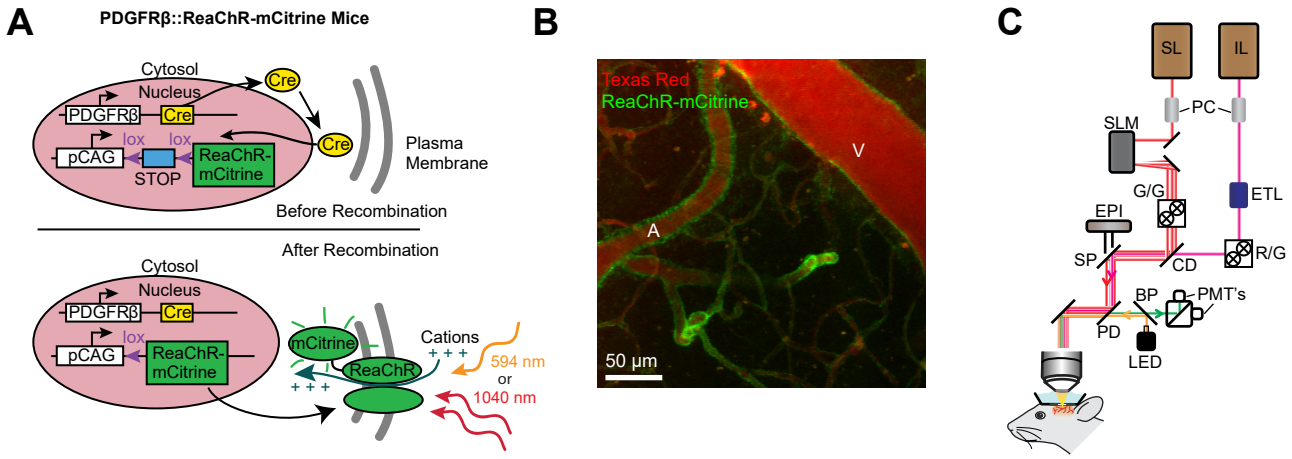

Figure 1. Mouse genetics and equipment for controlling arterial diameter with ReaChR. A. Crossing the PDGFRβ-Cre line with a floxed ReaChR (tagged with mCitrine) line leads to expression of the opsin in vascular mural cells. Mural cells can then be depolarized with single-photon excitation using a 594 nm LED or two-photon excitation with a fixed 1040 nm pulsed laser. Studies with control mice (see Figure 5-1) followed a similar strategy except only YFP was expressed in the cytosol of mural cells. **B.** Maximal projection image of cortical vessels from the mouse line created in panel A. The vascular lumen is labeled with Texas Red-dextran and the green in the vessel walls shows the expression of ReaChR-mCitrine. A=pial arteriole, V=pial venule. **C.** Imaging equipment - the Ultima 2P-Plus from Bruker (see Methods for details). Imaging laser (IL), Stimulation laser (SL), Pockel Cells (PC), Spatial Light Modulator (SLM), galvonometer mirrors (G/G), Electro-Tunable Lens (ETL), resonant scanning/galvonometer mirrors (R/G), combining dichroic (CD), primary dichroic (PD), LED (light-emitting diode) short-pass mirror (SP), band-pass mirror (BP), Photo-multiplier tubes (PMTs), epifluorescence module (EPI).

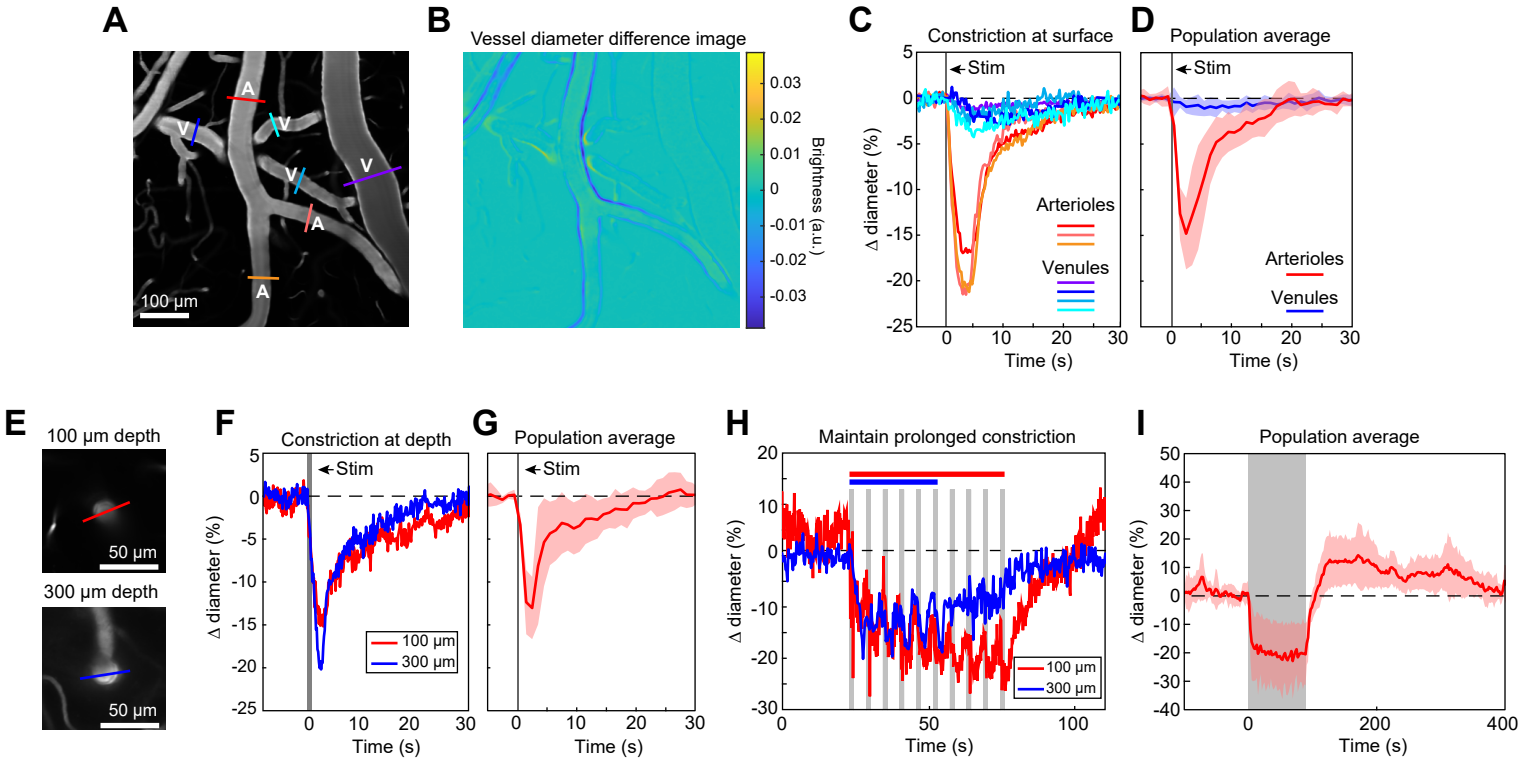

Figure 2. Full-field optogenetic activation of cortical vessels with 594 nm LED.
A. Cortical surface vessels labeled with FITC-dextran. Arterioles (A) and venules (V) are marked. **B.** Difference image created by subtracting the average of 4 seconds of data frames following stimulation (2.5 - 6.5 seconds after onset) from the average before stimulation (4 seconds before onset). Blue lines on vessel walls opposite each other indicate reduced brightness showing where constriction occurred. Vessels with yellow on one side and blue on the other indicate XY shifts in the image between the two intervals. Units are difference in arbitrary brightness values. **C.** Time courses of vessel diameter changes. Colored lines correspond to cross-sections in panel A, with arterioles in varying shades of red and venules in shades of blue. Vertical gray band is optical stimulation interval (100 ms pulse). **D.** Population average of 13 surface arterioles (red) and 10 surface venules (blue) from 3 mice stimulated with a single 100 ms pulse from the LED. Population constriction from 1-5 seconds following stimulation pulse: Arterioles = 11.1 ± 1%; Venules = 0.7 ± 0.2% (mean ± S.E.M.). **E.** Images of a penetrating arteriole 100 µm deep (top) and 300 µm deep (bottom) in the cortex. Colored cross-sections correspond to time course traces in F and H. **F.** A single train of LED light pulses (5 pulses, 100 ms, with 100 ms between) evoked strong constriction at both depths. **G.** Population average constriction of 5 penetrating arterioles from 3 mice to a single 100 ms pulse (8.6 ± 1.7%). **H.** We maintained vasoconstriction with repeated stimulation trains (5 pulses, 100 ms, 100 ms inter-pulse interval, 4 seconds between trains). Six trains were applied to the vessel at 300 µm and 10 to the vessel at 100 µm. **I.** Population average of 11 vessels (pial and penetrating arterioles were combined as responses were similar) from 3 mice to 90 seconds of continual LED light pulses (100 ms pulses, 0.4 Hz).

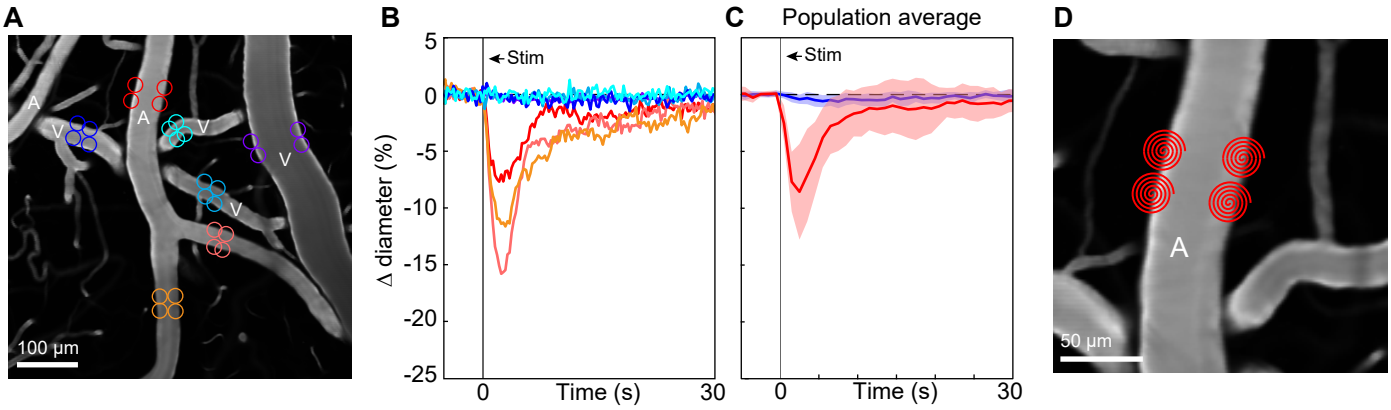

Figure 2-1. Two-photon optogenetic activation in venules versus arterioles.
A. Because venules showed small constriction to the full-field (single-photon) optogenetic stimulation (Figure 2B-D), we also tested the vessels with two-photon stimulation (1045 nm) targeted to individual vessel segments in separate runs. Colored circles indicate size and locations of stimulation spots and correspond to time courses in B. **B.** Time courses of diameter change following two-photon activation. Vertical gray band is optical stimulation interval (100 ms pulse). Arterioles were stimulated with ~110 mW total power. Venules were stimulated with up to ~330 mW and still no constriction was observed. **C.** Population average time course for surface arterioles (red) and venules (blue). Arterioles *N* = 8 vessels from 3 mice; Venules N = 11 vessels from same 3 mice. 4-6 spots, 20-25 µm in size were scanned on each vessel. Average total power for arterioles was 138 mW (range 90-250) and for venules was 245 mW (range 90-300). Population mean ± S.E.M. from 1-5 seconds following stimulation: Arterioles = 6.5 ± 1%; Venules = 0.4 ± 0.1%. **D.** Magnified view of the site of the red circles in A to show spiral pattern that was used to stimulate vessels. Circles are used throughout the paper for simplicity, but all spots were scanned in a 5-spiral pattern to activate more opsin molecules.

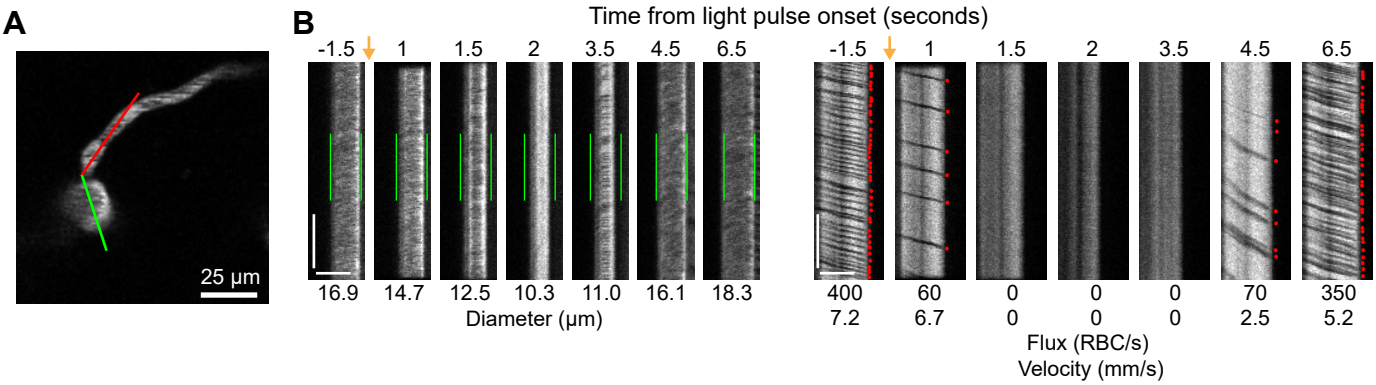

Figure 3. Optogenetic activation of vascular mural cells reduces blood flow.
A. Image of penetrating arteriole with an arteriole-capillary transition branch 85 µm below the surface. Line scans were acquired to measure the diameter of the arteriole (green segment) and the flow of the transition branch (red segment). A train of pulses (10 pulses, 100 ms, with 100 ms between) was delivered over the cranial window from the LED (594 nm). **B.** Line scan data from 7 time points during the run. Y-axis is time with each row being a single scan of the laser line. X-axis is distance along the line. The left set of panels shows the diameter data (the green segment in G) with the green bars indicating the pre-stimulus diameter. The right panels show the flow (the red segment in G) with each dot representing a single RBC passing through the segment (the dark streaks). The orange arrows indicate the interval when the light stimulus was applied. Numbers below each panel give the diameter of the penetrating arteriole and the flux and blood velocity for the transitional vessel. The arteriole constricts and flow is briefly eliminated (absence of dark spots in diameter segment at 2 seconds) before returning as the arteriole dilates back to the baseline level. Flow is reduced in the transition branch and then drops to zero (absence of dark streaks) before slowly recovering. Scale bars: Time axis: 25 ms; Distance axis: 25 µm.

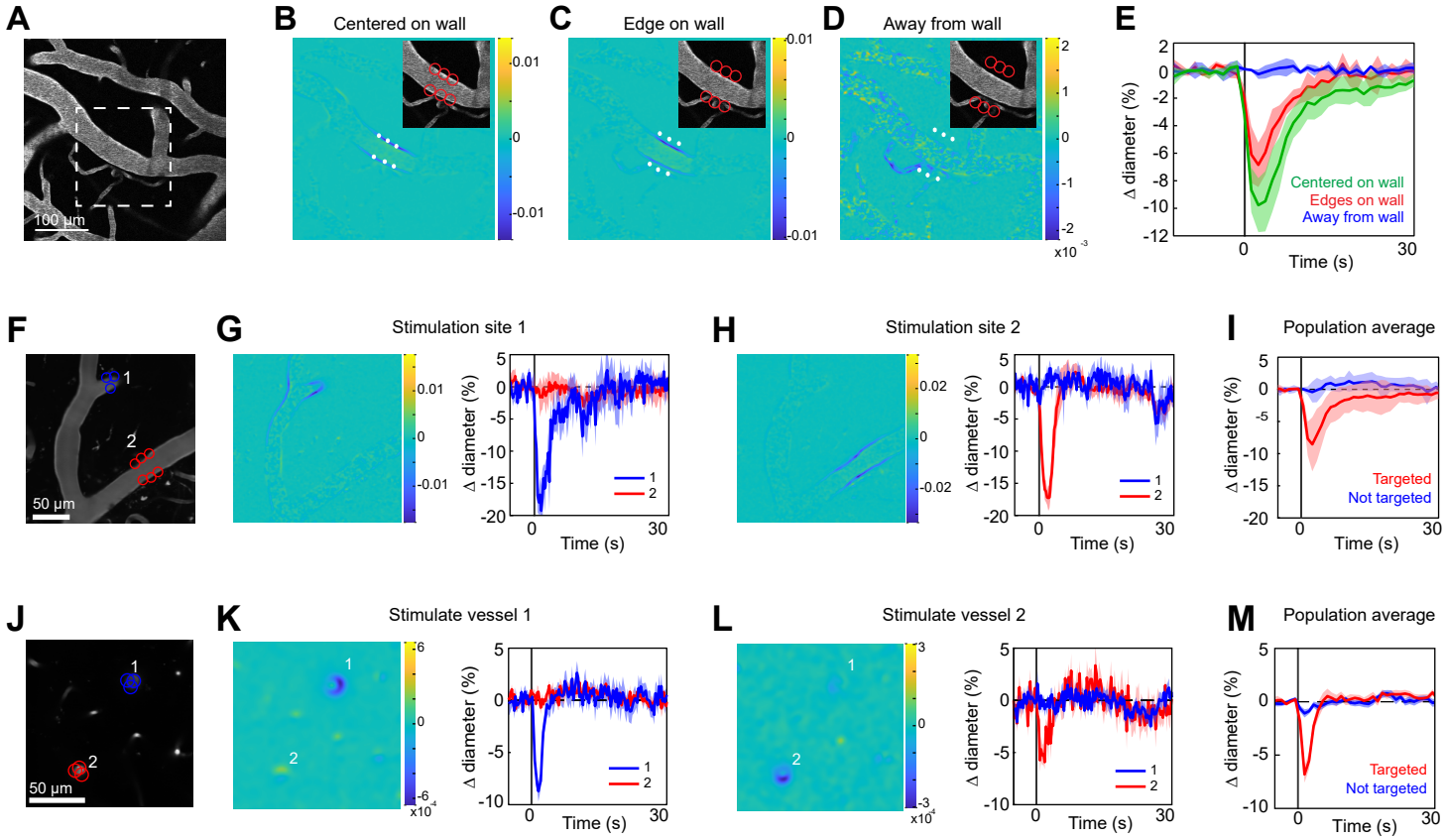

Figure 4. Spatial precision of two-photon optogenetic activation.

A-E. XY-precision of photostimulation. **A.** Image of surface vessels labeled with Texas Red-dextran in an opsin mouse that were photostimulated with spots in different positions relative to the vessel wall. Dashed rectangle indicates region in inset on the difference image panels (B-D). Three spot positions were used: **B** - spots centered on vessel walls, **C** - spot edges on vessel walls, and **D** - spot centers one diameter away from vessel walls. Difference images as in Figure 2. Red circles indicate the location and size of the spots, white asterisks indicate spot centers. **E.** Time courses of diameter changes based on spot position. Average of three vessels where this manipulation was performed, with 5 repetitions for each vessel. Error bands are standard deviation. Total laser power was ~130 mW divided between the 6 spots. Mean constriction for the three conditions was 0.0%, 4.8%, and 7.6% with S.E.M. <1% for all three conditions. **F-I.** Stimulation of different surface branches leads to isolated constriction. **F.** Surface vasculature labeled with Texas Red-dextran. Colored circles indicate size/location of stimulation spots and correspond to time course plots in G,H. For G, total laser power was ~90 mW. For H, total power was ~70 mW. **G,H.** Left panels: Difference images showing constriction (blue lines on both sides of vessel) only near stimulation points. Right panels: Time courses of diameter change for the two different stimulations: Error bands are standard deviation (SD) across five (G) or four (H) repetitions. Vertical gray band is stimulation interval (100 ms). **I.** Population average constriction of vessel segments targeted with stimulation (red) and when not targeted (blue). *N* = 8 vessels in 3 animals. Average total power per vessel was 138 mW (range 90-250 mW). Population mean ± S.E.M. from 1-5 seconds following stimulation: Targeted arterioles = 6.5 ± 1%; Untargeted = 0.3 ± 0.4%. **J-M.** Stimulation of penetrating arterioles with single-vessel precision. **J.** Two penetrating arterioles 200 µm below the cortical surface. **K-L.** Left panels: Difference images when stimulating arteriole #1 (K) or arteriole #2 (L). Each arteriole was stimulated with a total power ~110 mW. Right panels: Time courses of diameter change of the vessels indicated in the left panels. Data presented as mean and SD across 7 repetitions. **I.** Population average constriction of penetrating arterioles when targeted with stimulation (red) and when not targeted (blue). *N* = 9 vessels in 3 animals. Average total power applied to each vessel was 130 mW (range 80-190 mW). Population mean ± S.E.M. from 1.5-4.5 seconds following stimulation. Targeted arteries = 3.8 ± 0.6%; Untargeted = 0.7 ± 0.3%

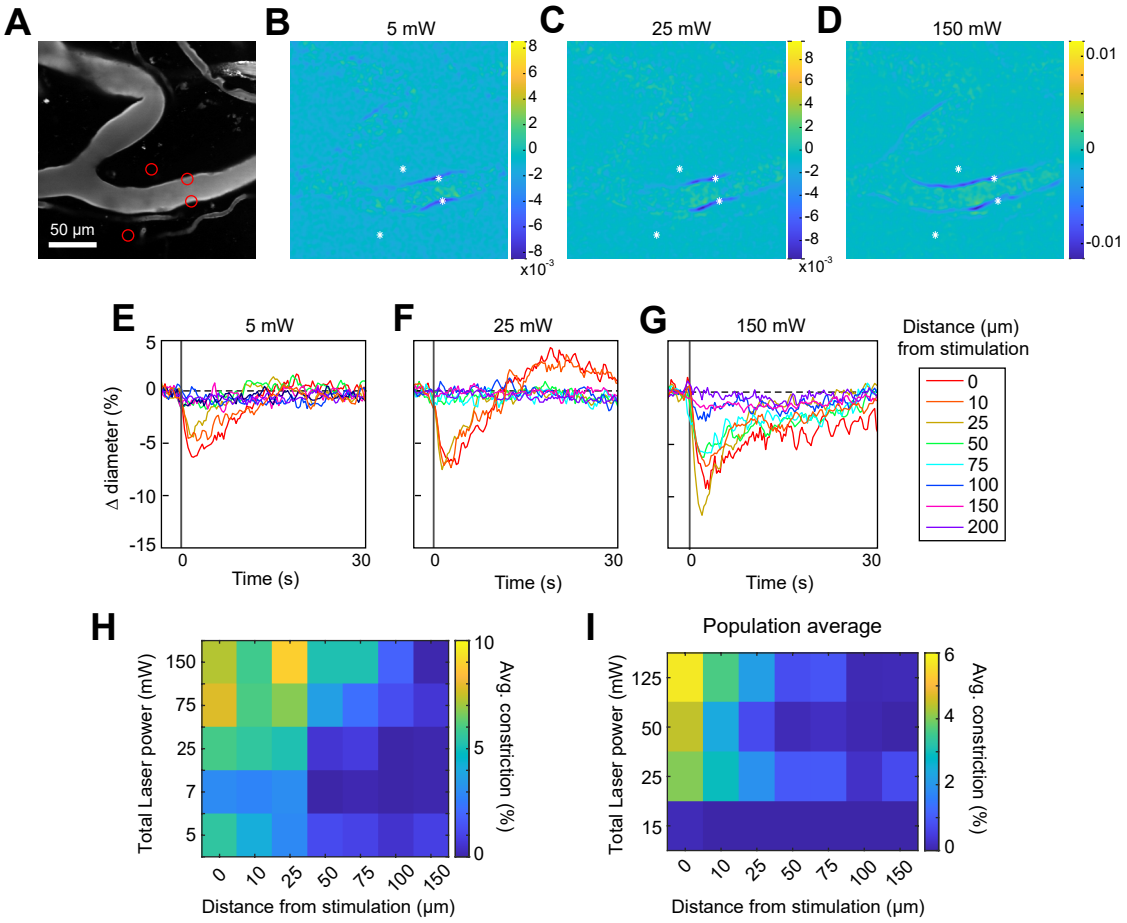

Figure 5. Effect of laser power on spread of constriction.
A. Vessels labeled with Texas Red-dextran. Red circles show spot size and location. Two spots off the vessel were to maintain similar power levels per spot compared to other runs (not shown). **B-D.** Difference images for three different power levels (values indicate total power of all 4 spots). **E-G.** Time courses of diameter change at the three power levels in B-D at different distances from the center of stimulation. **H.** Summary of constriction at all power levels tested across different distances. Average constriction from 1-5 seconds following stimulation onset (higher numbers/yellow color indicate greater constriction). **I.** Population average from 3 vessels in 3 mice of constriction at different power levels and distances from stimulation location. 6 spots were placed on vessels (15 µm, 3 on each side of vessel).

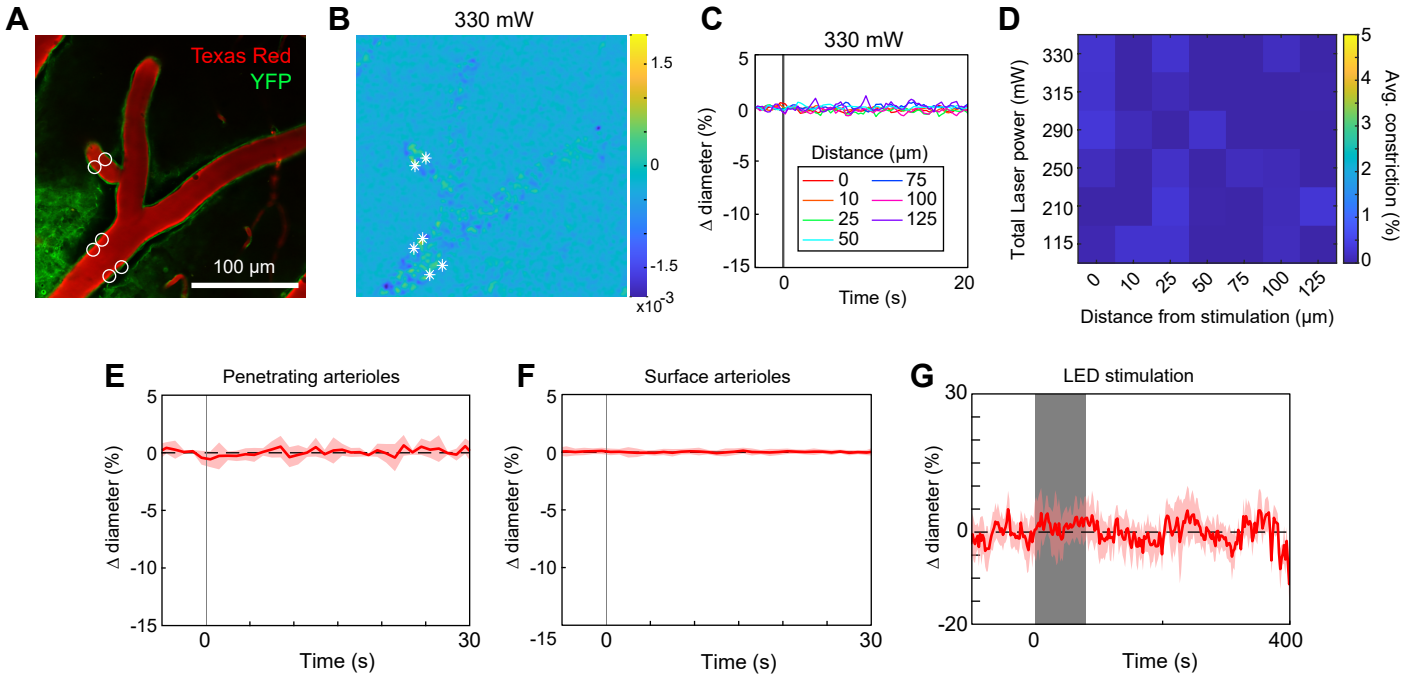

Figure 5-1. Control mouse expressing YFP only in mural cells exhibit no vasoconstriction. **A.** Control mice expressed yellow fluorescent protein (YFP) under control of the PDGFRβ promoter. Vessels labeled with Texas Red-dextran. White circles show spot size and location for two-photon optogenetic activation. **B.** Difference image for the maximum power level used (value indicates total power of all 6 spots). **C.** Time courses of diameter change at the maximum power level at different distances from the center of stimulation for the location with 4 spots on the arteriole. **D.** Summary of constriction at all power levels tested across different distances (color scale similar to Figure 5I for comparison). Even at very high powers, no constriction was seen. **E-G.** Population average for SLM stimulation of penetrating arterioles (**E**) and surface arterioles (**F**), and prolonged, repeated LED stimulation of surface and penetrating vessels combined (100 ms pulses, 0.25-0.43 Hz, 80-116 seconds) (**G**). N = 5 vessels from 2 mice (E), 19 vessels from 2 mice (F), 16 vessels from 3 mice (G).

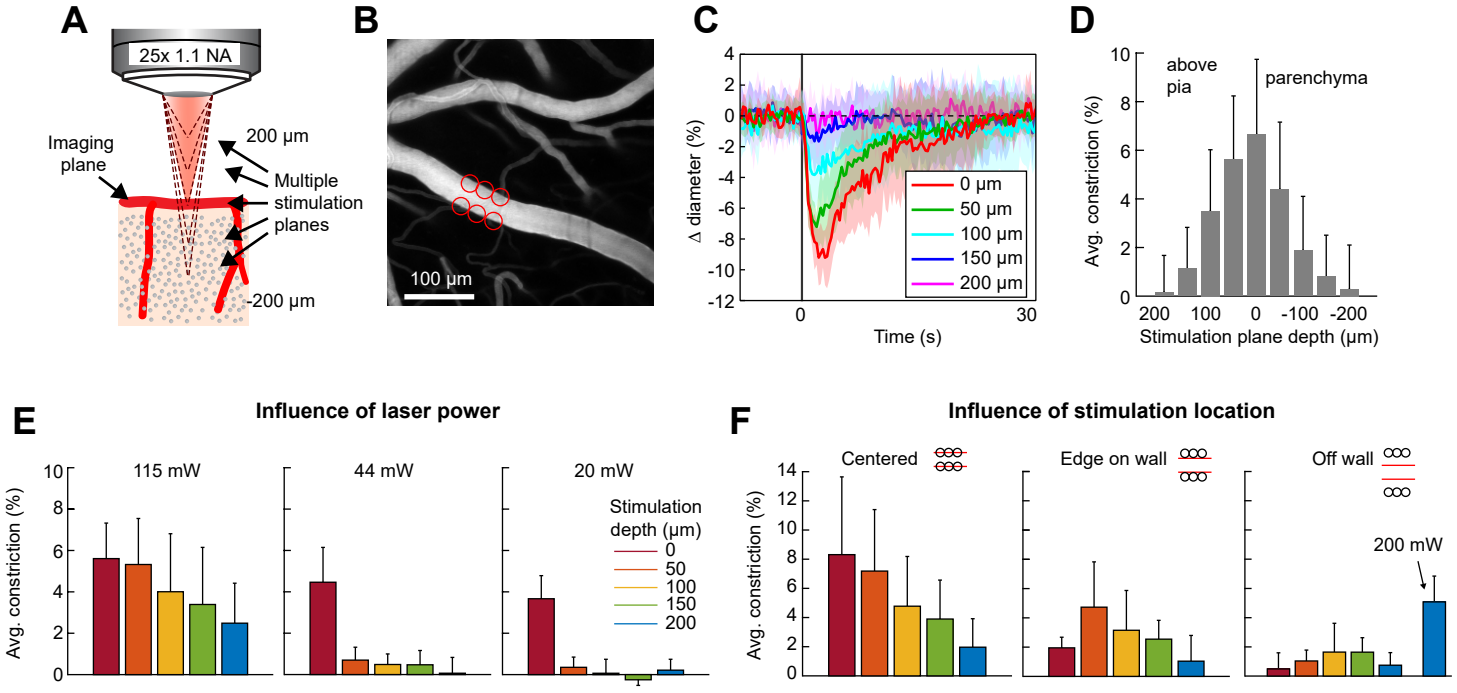

Figure 6. Axial resolution of two-photon optogenetic activation.
A. Schematic of imaging setup for measuring the axial resolution of two-photon activation. The objective focused the imaging beam on a pial arteriole at the cortical surface. The dashed lines indicate various focal planes of the stimulation laser generated by the SLM. In the experiment, stimulation spots were focused from 200 µm above to 200 µm below the imaging plane in 50 µm steps. **B.** Projection of surface vasculature labeled with Texas Red-dextran. Red circles indicate size and XY position of stimulation spots in varying depth planes. Total power was ~115 mW. **C.** Time courses of diameter changes following stimulation at different depths from the surface. Mean and SD across 8 repetitions. Equidistant planes above and below the surface were averaged together for visibility. **D.** Constriction amount at the different depths computed as the average change in diameter across repetitions from 1-5 seconds following the stimulation pulse. Error bars are SD across 8 repetitions. **E.** Axial resolution at three different total power levels averaged across 3 surface arterioles from 3 animals. Error bands are SD across vessels. **F.** Influence of stimulation spot location at different depths. 115 mW total power. N = 4 surface arterioles from 4 animals. For the “Off wall” condition, 200 mW total power was also used at the 200 µm depth.

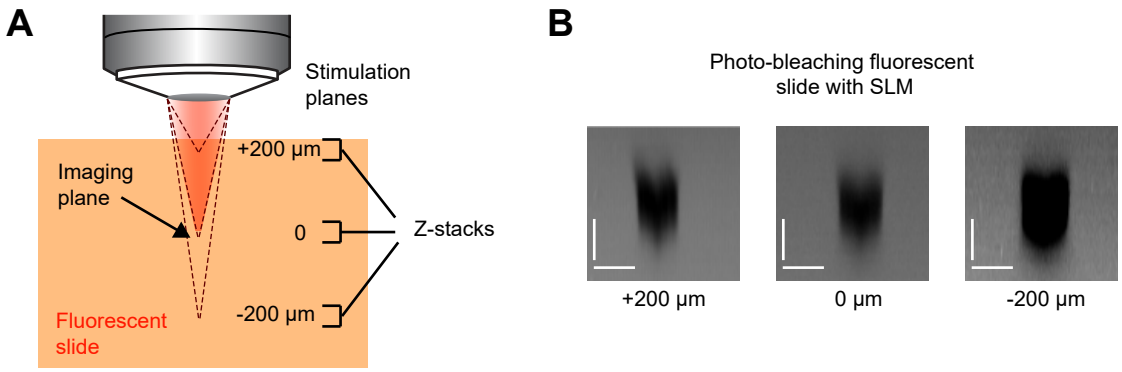

Figure 6-1. SLM focus test.
A. Schematic of a test to ensure the SLM focal plane was calibrated correctly. We focused the imaging laser beam in the middle of a fluorescent Chroma slide. We then used the SLM to place the stimulation laser at three different focal planes (the dashed lines). In separate runs, three stimulation spots (15 µm diameter) were focused 200 µm above, 200 µm below, or at the imaging plane, and high powers were delivered to bleach the fluorophore in the slide. Z-stacks were subsequently obtained with the imaging laser around one spot at each of the stimulation depths to determine the spread of the bleaching (and hence the spread of photo-stimulation). **B.** XZ-projections from the fluorescent slide. The region of photo-bleaching in the axial (Z) dimension was the same regardless of the SLM focus depth. Scale bars are 15 µm for both the axial and lateral dimensions.

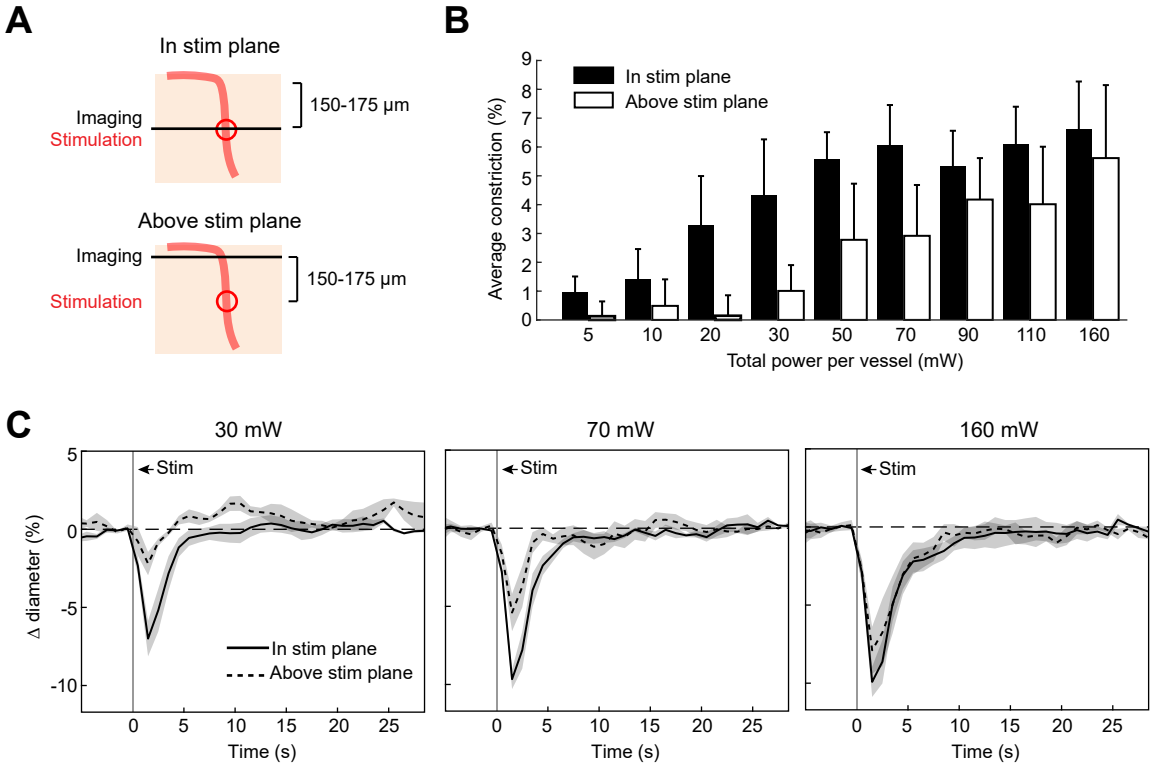

Figure 7. Axial spread of two-photon optogenetic activation.
A. Penetrating arterioles were stimulated using the SLM (100 ms light pulse) 200 µm below the surface while imaging was performed at the stimulation plane (top) or 150-175 µm above the stimulation plane (bottom). **B.** Average constriction from 0.5 - 3.5 seconds after stimulation across a range of powers. Three 15 µm diameter spots were placed on each arteriole and the total power to vessel is reported. **C.** Time course of constriction at the stimulation plane and above the stimulation plane for penetrating arterioles at three different stimulation power levels. Data for B and C are average and standard deviation (seven repetitions) of four arterioles from two mice.

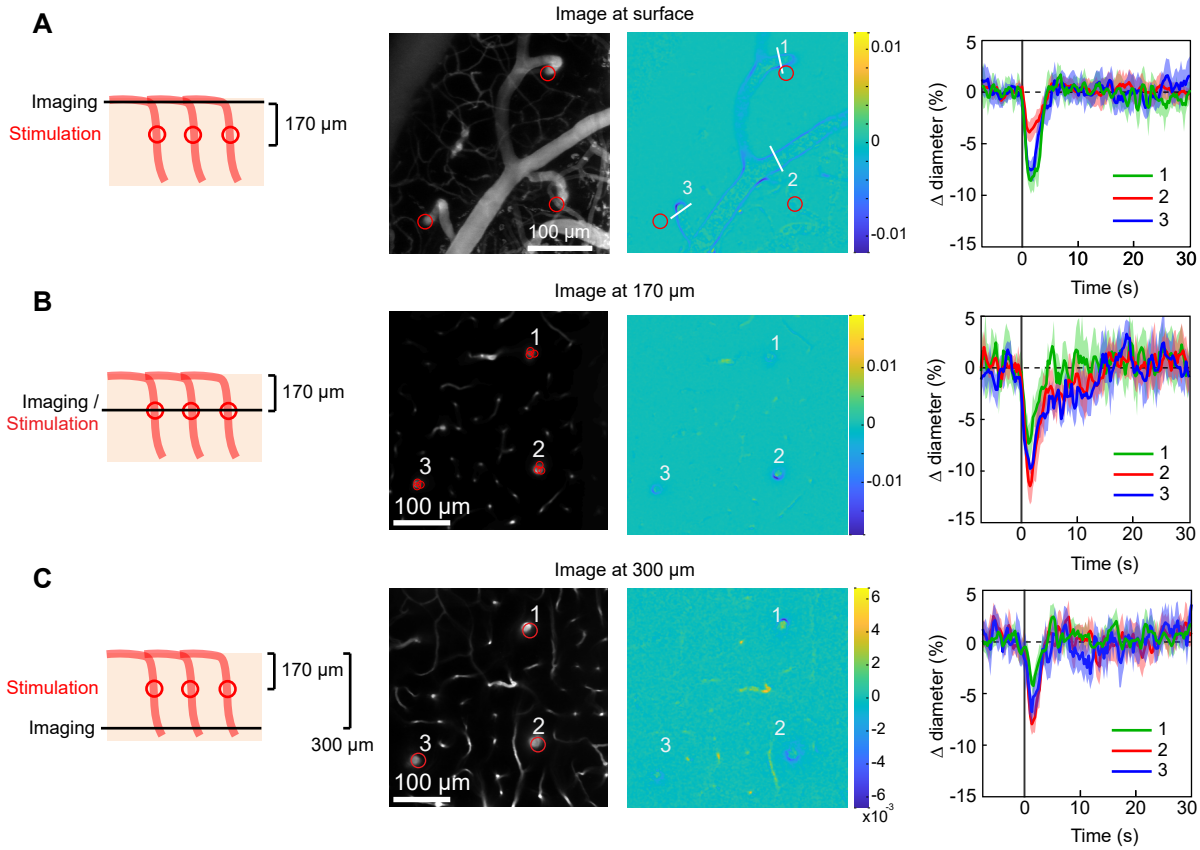

Figure 7-1. Broad axial constriction of penetrating arterioles with higher stimulation power.
A-C. Three penetrating arterioles were stimulated 170 µm below the surface while imaging at the cortical surface (A), in the stimulation plane (B) or 300 µm below the surface (C). Center-left panels show the Z-projection from the surface to 300 µm deep (A) or the single imaging plane (B-C). The red circles in A & C indicate the location of the three penetrating arterioles at the stimulation plane 170 µm below the surface. In B, the circles indicate the size and location of the stimulation spots. Total laser power to each arteriole was ~100 mW. Center-right panels are difference images. Right panels are time courses of constriction in the three vessels.

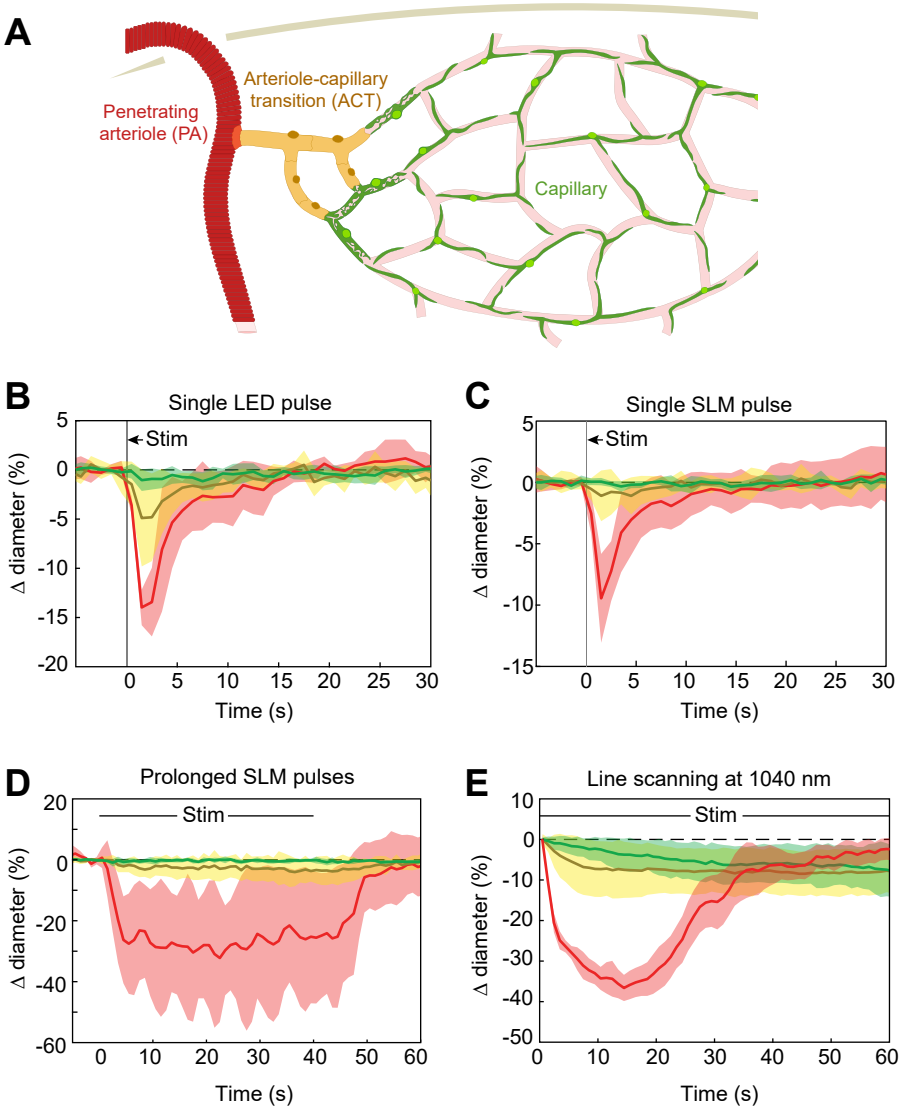

Figure 8. Optogenetic stimulation of vessels across microvascular zones.
A. Schematic showing three microvascular zones examined with different stimulation paradigms. **B.** Time course of constriction during a single 100 ms LED pulse (N=4 penetrating arterioles, N=6 ACT vessels, and N=9 capillaries). **C.** Time course of constriction during a single 100 ms pulse using the SLM (100-130 mW total power on each vessel) (N=7 penetrating arterioles, N=5 ACT vessels, and N=4 capillaries). **C.** Time course of constriction to repeated SLM pulses (100 ms pulses, 0.8-1.8 Hz, 40 seconds) (N=3 penetrating arterioles, N=6 ACT vessels, and N=5 capillaries). **D.** Time course of constriction to continuous line-scanning (N=9 penetrating arterioles, N=24 ACT vessels, and N=15 capillaries). Image collection and photo-excitation were simultaneously achieved with 1040 nm line scanning across vessels. Laser power varied from 10-120 mW with higher powers used for deeper vessels.

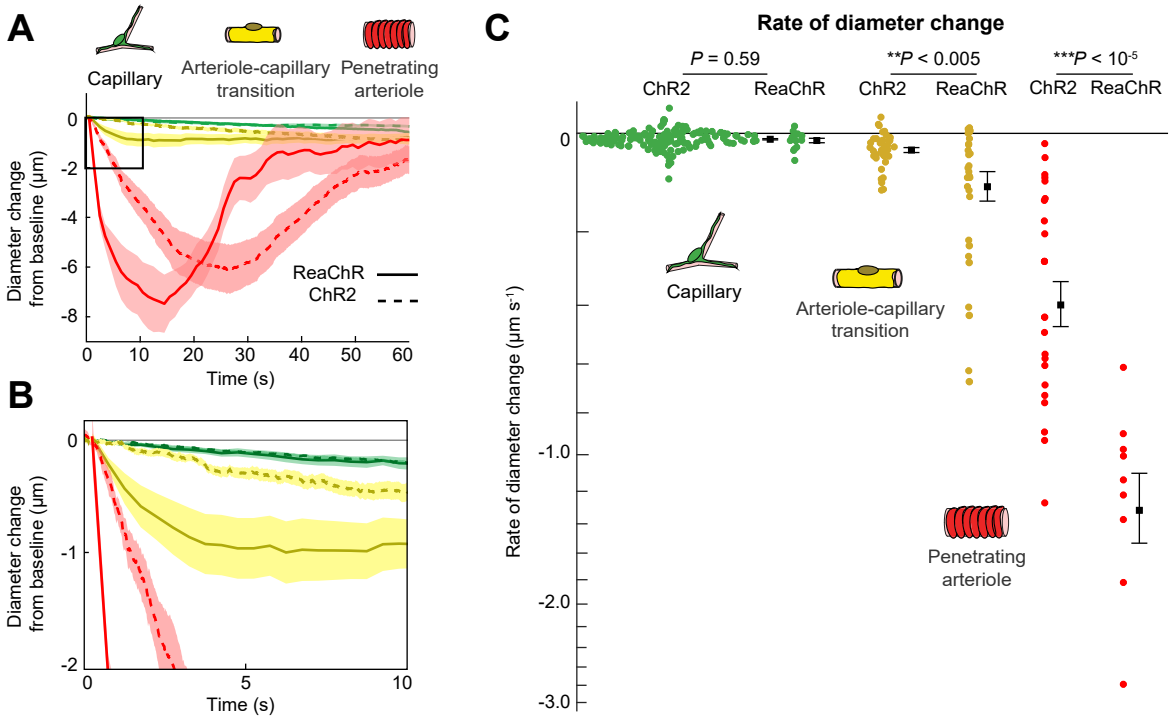

Figure 9. Comparison of ReaChR and ChR2 activation

A. Time course of constriction of three vessel classes covered by different mural cell types (ChR2 data from Hartmann et al. 2021; ReaChR data from line-scan stimulation in Figure 8E). Error bands are S.E.M.. Peak constriction time for penetrating arterioles: ReaChR = 14.5 seconds, ChR2 = 26 seconds. **B.** Inset showing zoomed view of the first 10 seconds of data. **C.** Rate of diameter change for each vessel computed over the first 10 seconds for capillaries and transitional vessels, and over the first 5 seconds for penetrating arterioles (because the constriction in the ReaChR arterioles had nearly plateaued by 10 seconds). Black squares and error bars are mean and S.E.M.. Results from One-way ANOVA on opsin type for each vessel class are shown. Mean values by group: Capillaries (-0.012 vs. -0.010 µm s^{-1} for ReaChR and ChR2 respectively); Transitional vessels (-0.10 vs. -0.03 µm s^{-1}); Penetrating arterioles (-1.31 vs -0.40 µm s^{-1}).

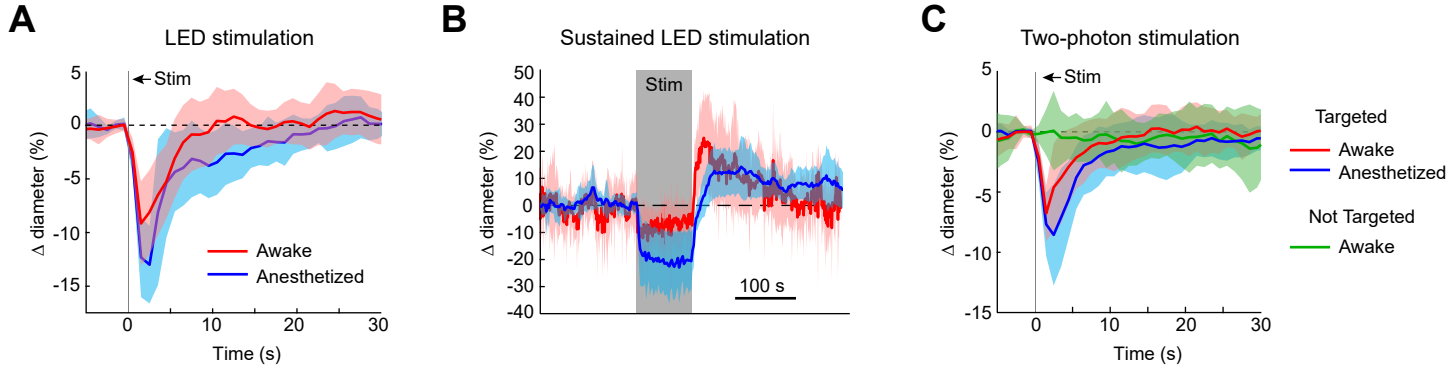

Figure 10. Optogenetic activation of vasculature in awake versus anesthetized mice.
A. Constriction of surface arterioles in awake and anesthetized mice to a 100 ms pulse from the LED. Anesthetized data from Figure 2D. Awake: *N* = 16 vessels in 2 animals. Population mean ± S.E.M. from 1-5 seconds following stimulation: 6.5 ± 0.6%. **B.** Constriction to prolonged repeated pulses (100 ms, 0.43-0.6 Hz, 56-145 seconds). Since different durations were used across animals, the time courses are aligned by onset and then by offset, and overlapped in the middle of the stimulation window. *N* = 14 vessels from 7 animals. Anesthetized data from Figure 2I. **C.** Single-vessel precision in awake animals. Average constriction of 14 vessels from 3 animals to a 100 ms pulse of two-photon stimulation using the SLM when targeted with the light (red) and when not targeted (green). Population mean ± S.E.M.: Targeted arteries = 4.3 ± 0.5%; Not targeted = 0.3 ± 0.5%. Anesthetized data from Figure 4I.

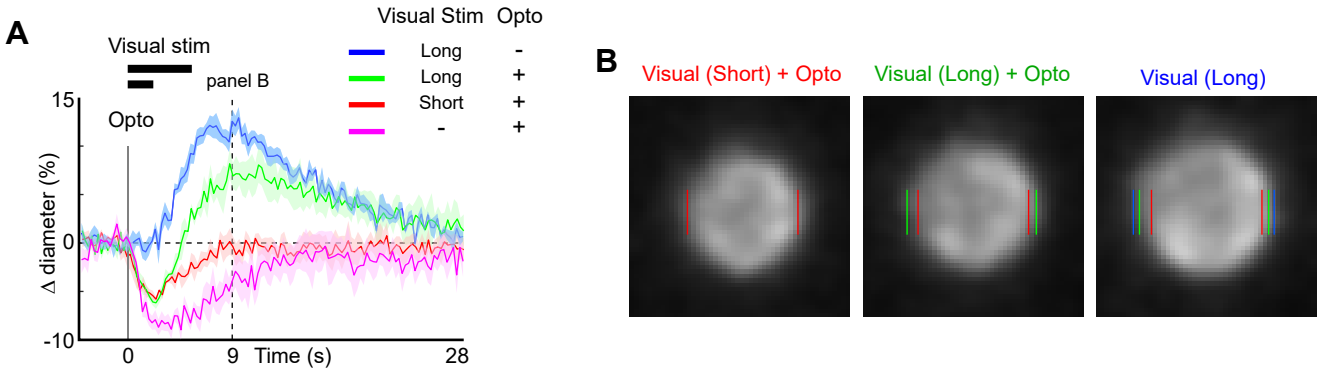

Figure 11. Modulation of sensory-evoked vasodilation using optogenetics

A. Pairing optogenetic stimulation with visual stimulation leads to reduced (green) or eliminated (red) visually-evoked dilations compared to visual stimulation alone (blue). Optogenetic stimulation with (red, green) or without (magenta) visual stimulation leads to constrictions much more rapidly than visually-evoked dilations. Vertical gray band at time 0 is optogenetic stimulation interval (100 ms) and black horizontal bars indicate visual stimulation duration (5 or 2 seconds, corresponding to long and short, respectively). Vertical dashed line at 9 seconds indicates time point of images shown in B. **B.** Single-frame images showing penetrating arteriole 9 seconds after stimulus onset for the conditions with visual stimulation. Colored lines indicate the computed diameter of the vessel cross-section in the image.

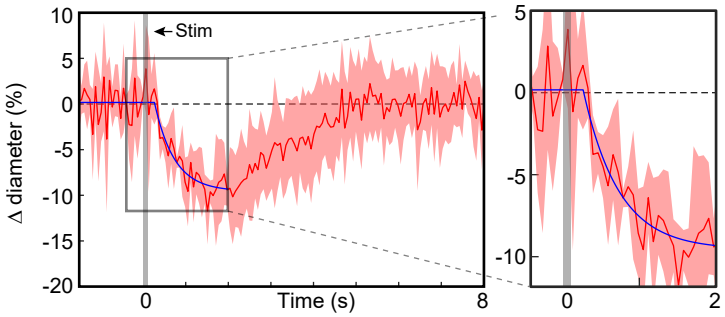

Figure 11-1. Speed of optogenetic constriction.
Time course of average of 5 arterioles that were imaged at high speed (15 Hz) to determine onset latency. Error band is standard deviation across runs. Blue curve is the fit to the data (see Methods). Vertical gray band is 100 ms light pulse. Right panel: Zoomed in view of plot around onset time for better visualization. Onset latency was computed as the point where the linear phase of the fit (baseline level) transitioned to the exponential phase (266 ms; 95% CI: 109-423 ms).

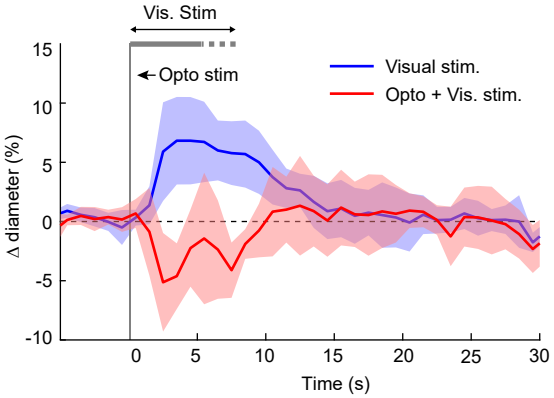

Figure 11-2. Offsetting functional hyperemia with optogenetic activation of mural cells - Population data. Population average (10 arterioles in 6 animals) diameter change to visual stimuli alone (blue) and when combined with optogenetic pulses (red: 1-3 100 ms pulses). Vertical gray band is the interval of the initial optogenetic stimulation pulse. Horizontal gray band is visual stimulus duration. The dashed right end indicates the range over which the visual stimuli ended in different animals (5-8 seconds). For a given vessel, the visual stimulus duration was the same in both conditions.

Movie Legends

Movie 1. Full-field activation with the 594 nm LED in a PDGFRβ/ReaChR mouse. Image is looking down at pial surface vessels in the neocortex labelled with FITC dextran. A single 100 ms pulse from the 549 nm LED was used to stimulate the vessels. In this and other movies, the dark flash indicates the time of the optical stimulation. The image darkens because the detectors are briefly blocked by mechanical shutters to protect them from the intense stimulation light. This and subsequent movies are presented at 4x real time.

Movie 2. Constriction of a penetrating arteriole 100 μm below the surface with the 594 nm LED. 5 pulses, 100 ms duration with 100 ms in between were presented.

Movie 3. The same vessel as Movie 2 was stimulated with 10 sets of 5 pulses, with 4 seconds between the onset of the pulse trains. Power and duration of pulses as in Movie 2.

Movie 4. Two-photon activation leads to focal constriction. The SLM focused 6 spots at the location indicated by the red arrow. The total stimulation power was ~200 mW spread over the 6 spots with 3 adjacent spots on either side of the vessel. Each spot was scanned in a 12 μm diameter spiral for 100 ms. The white arrow is for comparison with Movie 5. Vessels are labelled with Texas Red Dextran.

Movie 5. The same field-of-view as Movie 4 but here a different branch of the pial artery is stimulated (red arrow). Total power was ~75 mW spread out over 3 spots positioned on the branch stub and 3 off target spots. The white arrow indicates the location stimulated in Movie 4 for comparison.

Movie 6. Excessive laser power leads to vessel damage and widespread constriction. Same vessel as Figure 4A, here using a total of ~230 mW of laser power. The first pulse leads to a visibly damaged vessel wall and the second pulse breaks the wall causing dye leakage.

Movie 7. Control mouse expressing YFP in vessel walls shows that excessive laser power can lead to widespread constriction and vessel damage independently of opsins. The SLM focused 4 total spots, with pairs of spots opposite each other at the two different positions on the artery indicated by the arrows. The total stimulation power was ~265 mW, and each spot was scanned in a 12 μm diameter spiral for 100 ms.

Movie 8. Another example of vessel trauma at high powers in control mouse. Laser power was ~280 mW spread over 4 spots (pairs of spots opposite each other at arrow locations). .

Movie 9. Control mice show no constriction after light pulse when using powers that resulted in clear constrictions in ReaChR mice. Same site as Movie 7. The total stimulation power was ~200 mW.

Movie 10. Same as Movie 8 but the power was ~200 mW. No constriction is seen with the lower laser power.